

# Mapping stellar content to dark matter halos – III. Environmental dependence and conformity of galaxy colours

Ying Zu<sup>1,2\*</sup>, Rachel Mandelbaum<sup>2</sup>

<sup>1</sup>*Center for Cosmology and AstroParticle Physics (CCAPP), Ohio State University, Columbus, OH 43210, USA*

<sup>2</sup>*McWilliams Center for Cosmology, Department of Physics, Carnegie Mellon University, 5000 Forbes Avenue, Pittsburgh, PA 15213, USA*

Accepted XXX. Received YYY; in original form ZZZ

## ABSTRACT

Recent studies suggest that the quenching properties of galaxies are correlated over several mega-parsecs. The large-scale “galactic conformity” phenomenon around central galaxies has been regarded as a potential signature of “galaxy assembly bias” or “pre-heating”, both of which interpret conformity as a result of *direct* environmental effects acting on galaxy formation. Building on the iHOD halo quenching framework developed in Zu & Mandelbaum (2015, 2016), we discover that our fiducial halo mass quenching model, without any galaxy assembly bias, can successfully explain the overall environmental dependence and the conformity of galaxy colours in SDSS, as measured by the mark correlation functions of galaxy colours and the red galaxy fractions around isolated primaries, respectively. Our fiducial iHOD halo quenching mock also correctly predicts the differences in the spatial clustering and galaxy-galaxy lensing signals between the more vs. less red galaxy subsamples, split by the red-sequence ridge-line at fixed stellar mass. Meanwhile, models that tie galaxy colours fully or partially to halo assembly bias have difficulties in matching all these observables simultaneously. Therefore, we demonstrate that the observed environmental dependence of galaxy colours can be naturally explained by the combination of 1) halo quenching and 2) the variation of halo mass function with environment — an *indirect* environmental effect mediated by two separate physical processes.

**Key words:** cosmology: observations — cosmology: large-scale structure of Universe — gravitational lensing: weak — methods: statistical

## 1 INTRODUCTION

Recent studies have shown that the quenching (i.e., the cessation of star forming activities in galaxies) properties of central galaxies, such as star formation rate (SFR), morphology, neutral hydrogen content, and broad-band colour, are correlated with those of their neighbouring galaxies (Weinmann et al. 2006; Yang et al. 2006; Ann et al. 2008; Kauffmann et al. 2010; Prescott et al. 2011; Kauffmann et al. 2013; Knobel et al. 2015; Hartley et al. 2015; Wang et al. 2015; Kawinwanichakij et al. 2016; Berti et al. 2017). This so-called “galactic conformity” phenomenon exists over two distinct distance scales between the central galaxy of a primary dark matter halo and its surrounding galaxies, including the true satellite galaxies within the same halo ( $<0.5 h^{-1}\text{Mpc}$ ;

first detected by Weinmann et al. 2006)<sup>1</sup>, and galaxies in halos that are a few virial radii away from the primary ( $\sim 3 h^{-1}\text{Mpc}$ ) — effects we refer to as “1-halo” and “2-halo” conformities, respectively. In essence, galactic conformity is a manifestation of some unknown environmental effect on galaxy formation, and is closely related to the colour-density or morphology-density relation that has been known for many decades (Oemler 1974; Dressler 1980). However, it is not clear whether galactic conformity extends to even larger scales, and the underlying driver of this environmental effect remains one of the most important open questions in galaxy formation theory.

The 1-halo conformity is closely related to the physics of galaxy quenching within individual halos. For instance, virial shocks can heat the incoming gas to high tempera-

<sup>1</sup> Weinmann et al. (2006) compared group-sized halos at fixed total optical luminosity, which they used as a proxy for halo mass.

\* E-mail: zu.4@osu.edu

tures and inhibit star formation if the halo is more massive than a few  $\times 10^{12} h^{-1} M_{\odot}$  (Birnboim & Dekel 2003; Cattaneo et al. 2006; Dekel & Birnboim 2006; Ocvirk et al. 2008; Kereš et al. 2009). Massive clusters can even drive extended distribution of hot halo gas via accretion shocks up to several times the virial radii (Bahé et al. 2013; Gabor & Davé 2015; Zinger et al. 2016). Feedbacks from active galactic nucleus (AGN) can also potentially truncate the merger-driven star formation episodes at high redshift (Di Matteo et al. 2005; Hopkins et al. 2005), and keep the hot gas from cooling efficiently at low redshift (Croton et al. 2006; Fabian 2012; Cheung et al. 2016). In addition, the hot halo gas can strip the gaseous disks from newly accreted satellites (Gunn & Gott 1972; McCarthy et al. 2008; Font et al. 2008), while transforming spirals into S0 galaxies (Bekki et al. 2002). The efficiencies of all those physical processes are directly tied to the halo mass, and we will collectively refer to them as “halo quenching”.

Recently, from the weak lensing measurements of the locally brightest galaxies in the Sloan Digital Sky Survey (SDSS; York et al. 2000), Mandelbaum et al. (2016) discovered a strong bimodality in the average host halo mass of the red vs. blue central galaxies — at fixed  $M_*$ , red central galaxies preferentially live in halos that are factor of two ( $M_* \sim 2 \times 10^{10} h^{-2} M_{\odot}$ ) to almost ten ( $M_* > 2 \times 10^{11} h^{-2} M_{\odot}$ ) more massive than ones that host blue centrals (see also Mandelbaum et al. 2006; More et al. 2011). Zu & Mandelbaum (2016) interpreted this halo mass bimodality as a pronounced signature of halo quenching, and demonstrated that models without an explicit halo quenching are unlikely able to reproduce such strong bimodality in halo mass. For example, in a model that maximizes the so-called “galaxy assembly bias” (Zhu et al. 2006; Croton et al. 2007; Zu et al. 2008; Zentner et al. 2014) by matching galaxy colours to the formation time of halos (i.e., age-matching; Hearin & Watson 2013), blue central galaxies are instead placed in slightly more massive halos than red centrals, due to the weak anti-correlation between the formation time and mass of halos.

The observed 1-halo conformity effects are consistent with the halo quenching scenario. Wang & White (2012) found qualitative agreement between the 1-halo colour conformities observed in SDSS and predicted by the Guo et al. (2011) semi-analytic model (SAM), where star formation is regulated by the AGN “radio-mode” feedback with an efficiency that is directly tied with halo mass  $M_h$  (Croton et al. 2006). Using morphology as the quenching indicator, Ann et al. (2008) found a similar 1-halo conformity effect in SDSS and argued that the hot halo gas in high-mass systems could be responsible for the coherent transformation of galaxy morphologies.

In the 2-halo regime, a possible conformity effect was first detected by Kauffmann et al. (2010) using photometrically-selected satellite galaxies in SDSS. Switching to the spectroscopic satellite sample, Kauffmann et al. (2013) found that for primaries with  $M_*$  around a few  $\times 10^{10} h^{-2} M_{\odot}$ , strong conformity between the gas-poor primaries and the HI content of satellites persists at projected distances of  $\sim 3 h^{-1} \text{Mpc}$ , where a direct causal link between the two becomes unlikely; for primaries with  $M_* \sim 10^{11} h^{-2} M_{\odot}$ , the large-scale conformity signal is weak and confined within a couple virial radii of clusters.

One potential problem with the 2-halo conformity detection is, the primary galaxies in Kauffmann et al. (2013) were selected by an isolation criteria that could include gas-poor low-mass central galaxies within the vicinity of a massive companion (Stark et al. 2016), or even mis-identify a small fraction of satellites within a larger system as primaries (Tinker et al. 2017). Kauffmann et al. (2013) explored this contamination issue using the Guo et al. (2011) SAM mock catalogue, and argued that the impact is too small to account for the observed conformity. However, using a group finding algorithm for identifying centrals, Tinker et al. (2017) argued that the 2-halo conformity seen by Kauffmann et al. (2013) could be artificially boosted by the mis-identified primaries in the sample. Sin et al. (2017) also discovered that the isolation criteria of Kauffmann et al. could include low-mass central galaxies in the vicinity of massive systems, and that the large-scale conformity signal is likely a short-range effect sourced by massive halos.

Currently, there are two possible explanations of the 2-halo conformity effect. Kauffmann et al. (2013) argued that the strong signal around the very low-mass central galaxies (a few  $\times 10^9 h^{-2} M_{\odot}$ ) favors the “pre-heating” scenario in which large reservoirs of intergalactic medium (IGM) was heated up to a high entropy level, probably due to bursty star-forming activities at early epochs or spatially-coherent injection of energy from AGN/stellar feedbacks (Mo & Mao 2002). Despite the lack of robust detections so far (see Yang et al. 2006; Lin et al. 2016; Vakili & Hahn 2016), the galaxy assembly bias effect can also produce a strong 2-halo conformity signal, by making use of the coupling between halo accretion histories in the same density environment across large scales (Hearin et al. 2015). In essence, both pre-heating and galaxy assembly bias are *direct* environmental effects on two key parameters of galaxy formation, i.e., the entropy of IGM and the overall accretion rate of baryons, respectively.

Alternatively, an *indirect* environmental effect, such as the combination of the environmental dependence of halo mass function and the simple halo quenching mechanism, should also give rise to a large-scale galactic conformity. This third, indirect effect has not been adequately explored in previous studies, partly due to a common mis-conception that there is no inherent environmental dependence in the standard halo model framework (Cooray & Sheth 2002). But as articulated by Martino & Sheth (2009) (see also Mo & White 1996; Lemson & Kauffmann 1999; Sheth & Tormen 2002), the dependence of halo abundance and formation history on the large-scale density environment is a standard element of the excursion set theory of cosmological structure formation (Press & Schechter 1974; Bond et al. 1991; Lacey & Cole 1993), which also allows mass-dependent biasing to be understood within the peak-background split formalism (Bardeen et al. 1986; Sheth & Tormen 1999).

Is halo quenching consistent with the environmental dependence of colours observed in SDSS? In the pioneering work by Skibba & Sheth (2009), they demonstrated that a simple Halo Occupation Distribution (HOD; Jing et al. 1998; Ma & Fry 2000; Peacock & Smith 2000; Seljak 2000; Yang et al. 2003; Scoccimarro et al. 2001; Berlind & Weinberg 2002; Guzik & Seljak 2002; Zheng et al. 2005; Mandelbaum et al. 2006; van den Bosch et al. 2007; Ross & Brunner 2009; Leauthaud et al. 2012; Zu & Mandelbaum 2015) model of galaxy colours, without assembly bias, is able to reproduce

the level of environmental dependence of colours in SDSS up to  $20 h^{-1}\text{Mpc}$ . They are the first to employ the mark correlation functions of colours as a robust measure of the environmental dependence of galaxy quenching, which includes contributions from the large-scale conformity around central galaxies and the correlation between the colours of satellites inside different halos. However, Skibba & Sheth (2009) made a few overly-simplified assumptions, including that the galaxy colour depends solely on luminosity. As a result, this model does not represent a viable halo quenching model, and is thus unlikely able to explain the observed strong halo mass bimodality of central galaxies in SDSS (Zu & Mandelbaum 2016).

Similarly, Hearin et al. (2015) constructed an HOD mock of galaxy colours that has the similar  $M_h$ -dependence of red galaxy fractions as their age-matching mock, but without any galaxy assembly bias. They found that this HOD mock does not produce any conformity effects, as measured by the red galaxy fractions around the red vs. blue primaries selected in the same way as in Kauffmann et al. (2013). Hearin et al. (2015) further argued that a large-scale conformity signal is the smoking-gun evidence of galaxy assembly bias. However, despite the technical differences between the HOD mocks built by Skibba & Sheth (2009) and Hearin et al. (2015), it is quite intriguing that a strong overall environmental dependence of colours seen in one may not yield an equally strong conformity signals of centrals in the other.

Therefore, it is very important to explore whether a viable halo quenching model within the HOD framework can simultaneously explain the environmental effects in the spatial distribution of galaxy colours and the large-scale colour conformity signals observed in SDSS. In this paper, we build on the best-fitting halo quenching model within the iHOD framework developed in our Paper I (Zu & Mandelbaum 2015) and II (Zu & Mandelbaum 2016) of this series, and employ the mark correlation functions and the red galaxy fractions at fixed  $M_*$  as the joint probe of environmental effects in our analysis. To better distinguish different models of galaxy colours, we also investigate the spatial clustering and the g-g lensing of more vs. less red galaxies, split by the red-sequence (RS) ridge-line at fixed  $M_*$ .

This paper is organized as follows. We briefly describe the iHOD framework and the simple halo quenching model in § 2, and introduce our three colour assignment schemes in § 3. We present our main findings in § 4 and conclude by summarizing our results and looking to the future in § 5.

## 2 THE iHOD MODEL AND MOCK GALAXY CATALOGUES

The mock galaxy catalogues in this study are built on the iHOD model developed in Papers I & II. We will briefly describe the main features of iHOD below, and refer readers to Papers I & II for more details, including the mathematical framework of the model, the selection of galaxy samples from SDSS, and the measurement of  $w_p$  and  $\Delta\Sigma$  for those samples. We will also describe the  $N$ -body simulations and procedures we employ to generate the mock galaxy catalogues. Readers who are familiar with Papers I & II can skip the next subsection and start from § 2.2.

For the conformity “mark” we focus on the  $g-r$

colours ( $K$ -corrected to  $z=0.1$ ), which are measured much more robustly than other quenching indicators like the SFR or HI gas mass. Studies of environmental effects are particularly sensitive to the volume size, and Xu et al. (2016) demonstrated that the clustering of low- $M_*$  galaxies in the local volume below  $z=0.03$  are subjected to very severe cosmic variance effect. Therefore, we limit our analyses to galaxies with  $M_* \geq 10^{10} h^{-1} M_\odot$ , so that the minimum redshift range of our volume-limited galaxy samples is  $z=[0.01, 0.07]$ , i.e., the redshift range of our lowest- $M_*$  sample. The maximum redshift probed by the high- $M_*$  samples is 0.2, and the median redshift of the SDSS galaxies used this analysis is around 0.1.

Throughout this paper and Papers I & II, all the length and mass units are scaled as if the Hubble constant were  $100 \text{ km s}^{-1} \text{ Mpc}^{-1}$ . In particular, all the separations are expressed in co-moving distances in units of either  $h^{-1} \text{ kpc}$  or  $h^{-1} \text{ Mpc}$ , and the stellar masses and halo masses are in units of  $h^{-2} M_\odot$  and  $h^{-1} M_\odot$ , respectively. We employ the stellar mass estimates from the latest MPA/JHU value-added galaxy catalogue<sup>2</sup>, and convert other stellar masses (e.g., in the age-matching mock of Hearin et al. 2014) to the MPA/JHU values using the fitting formulae given by Li & White (2009). Unless otherwise noted, the halo mass is defined by  $M_h \equiv M_{200m} = 200 \bar{\rho}_m (4\pi/3) r_{200m}^3$ , where  $r_{200m}$  is the corresponding halo radius within which the average density of the enclosed mass is 200 times the mean matter density of the Universe,  $\bar{\rho}_m$ .

### 2.1 The iHOD Model and Simple Halo Mass Quenching

The iHOD framework aims to describe the *probabilistic* connection between galaxies and halos, assuming that the enormous diversity in the individual galaxy assembly histories inside similar halos would reduce to a stochastic scatter about the *mean* galaxy-to-halo relation by virtue of the central limit theorem. Therefore, the key is to derive  $P(\mathbf{g} | \mathbf{h})$ , the conditional probability distribution function (PDF) of galaxy properties  $\mathbf{g}$  at fixed halo properties  $\mathbf{h}$ , where  $\mathbf{g}$  and  $\mathbf{h}$  are the corresponding vectors that describe the most important sets of galaxy and halo properties. For example, we could include stellar mass, optical colour, SFR, and morphology in  $\mathbf{g}$ , and halo mass, concentration, spin, and tidal environment in  $\mathbf{h}$ .

In Paper I and II, we have applied the iHOD model to the SDSS main spectroscopic sample, and successfully mapped the red and blue galaxies at different stellar masses to their underlying halos. In this first-cut analysis, we adopted a binary colour variable  $b_{g-r}$ , by classifying each galaxy into either red ( $b_{g-r}=1$ ) or blue ( $b_{g-r}=0$ ) based on a  $M_*$ -dependent colour-split

$$(g-r)_{\text{split}} | M_* = 0.8 \left( \frac{\lg M_*}{10.5} \right)^{0.6}. \quad (1)$$

We then derived the conditional probability distribution of halo mass for galaxies at fixed stellar mass and colour category  $P(M_h | M_*, b_{g-r})$ , from the stellar mass and color dependence of galaxy clustering ( $w_p$ ) and g-g lensing ( $\Delta\Sigma$ ) mea-

<sup>2</sup> <http://home.strw.leidenuniv.nl/~jarle/SDSS/>

surements. Thanks to the probabilistic nature of the model, we are able to include  $\sim 80\%$  more galaxies in the analysis than traditional HOD methods, while accounting for the incompleteness of galaxy samples in a statistically consistent fashion.

In practice, we first derive the overall stellar-to-halo connection  $P(M_h | M_*)$  in Paper I from the stellar mass dependence of  $w_p$  and  $\Delta\Sigma$ . In Paper II, we describe the halo quenching effect statistically using the red galaxy fractions of centrals and satellites as functions of  $M_h$  (c.f. equations 12 and 13 of Paper II),

$$f_{\text{cen}}^{\text{red}}(M_h) = 1 - f_{\text{cen}}^{\text{blue}}(M_h) = 1 - \exp\left[-\left(M_h/M_h^{qc}\right)^{\mu^c}\right], \quad (2)$$

and

$$f_{\text{sat}}^{\text{red}}(M_h) = 1 - f_{\text{sat}}^{\text{blue}}(M_h) = 1 - \exp\left[-\left(M_h/M_h^{qs}\right)^{\mu^s}\right], \quad (3)$$

where  $M_h^{qc}$  and  $M_h^{qs}$  are the critical halo masses responsible for triggering quenching of central and satellites, respectively, and  $\mu^c$  and  $\mu^s$  are the respective powered-exponential indices controlling the transitional behavior of halo quenching across the critical halo masses. Therefore, by combining Equations 2 and 3 together with the overall  $P(M_h | M_*)$ , we now arrive at a complete model for  $P(M_h | M_*, b_{g-r})$ .

More importantly, the best-fitting  $P(M_h | M_*, b_{g-r})$  successfully predicts the strong bimodality in the host halo mass distributions of the red and blue galaxies in SDSS (Mandelbaum et al. 2016), which implies a dominant halo quenching mechanism that turns on in halos above  $M_h^{qc} \simeq M_h^{qs} \simeq 1.5 \times 10^{12} h^{-2} M_\odot$  (with different powered-exponential indices for central and satellites). This success is highly non-trivial, as many alternative models that strive to explain galaxy colours fail this test (e.g., by assigning galaxy colours based on halo age or stellar mass; Zu & Mandelbaum 2016).

One of the interesting extensions of the current iHOD model, expressed by  $P(M_h | M_*, b_{g-r})$ , is to add an important secondary halo property, such as concentration  $c$ , to see whether it would provide a more comprehensive description of the observed galaxy colours, especially when  $g-r$  is included as a continuous variable instead of a binary one. This extension, expressed by  $P(M_h, c | M_*, g-r)$ , also represents a useful formalism for including galaxy assembly bias when connecting galaxy colours to halos, because concentration is one of the best indicators for halo assembly bias (see also Paranjape et al. 2015; Rodríguez-Puebla et al. 2016; Hearin et al. 2016; Pahwa & Paranjape 2016; Rodríguez-Puebla et al. 2017).

## 2.2 From iHOD to Mock Galaxy Catalogues

In Papers I & II we adopted an analytic method to predict the projected galaxy correlation function  $w_p$  and  $g$ - $g$  lensing signal  $\Delta\Sigma$  at fixed  $M_*$  for the red and blue galaxies in SDSS. In this paper, a fully analytic approach will not enable us to easily address the question of interest, so we will predict  $w_p$ ,  $\Delta\Sigma$ , as well as the colour-mark correlation function  $M_{g-r}$  and the red galaxy fraction as a function of projected distance  $f_{\text{red}}(R)$  using direct measurements from the mock galaxy catalogues generated under iHOD (but see Sheth 2005, for an analytic halo-model description of  $M_{g-r}$ ).

In order to cover a dynamic range of two orders of

magnitude in stellar mass ( $10^{10}$ - $10^{12} h^{-2} M_\odot$ ), we employ two cosmological  $N$ -body simulations that are evolved from the same *WMAP5* cosmological parameters (Komatsu et al. 2009), but with complementary sets of mass resolutions and volumes. For mock galaxies with  $\lg M_* < 10.6$ , we use the Bolshoi (Klypin et al. 2011) simulation because of its higher mass resolution ( $1.35 \times 10^8 h^{-1} M_\odot$ ). The volume of Bolshoi is too small ( $250^3 h^{-3} \text{Mpc}^3$ ) to overcome the cosmic variance of more massive galaxies, so we use the MDR1 simulation ( $8.721 \times 10^9 h^{-1} M_\odot$  particle mass and a  $1 h^{-3} \text{Gpc}^3$  box; Prada et al. 2012) for deriving mock galaxies with  $\lg M_* \geq 10.6$ . In both simulations, we make use of the halo catalogues identified by the ROCKSTAR (Behroozi et al. 2013) spherical overdensity halo finder at  $z=0.1$ , the median redshift of our SDSS galaxy samples.

Since the cosmology assumed in Papers I & II is slightly different from the *WMAP5* values used by the simulations, we have re-calculated the constraints on the global iHOD parameters and the halo quenching model using the *WMAP5* cosmology. We have also updated our analytic model in Paper I by including the so-called ‘‘residual redshift-space distortion’’ effect in  $w_p$ , using the correction method described in van den Bosch et al. (2013). The main change in cosmology is the increase of  $\sigma_8$ , which we anticipate to affect primarily  $\delta$ , the high-mass end slope of the mean stellar-to-halo mass relation (SHMR), but cause very little change to the slope at the low-mass end or the scatter about the mean SHMR (Leauthaud et al. 2012; Zu & Mandelbaum 2015). Therefore, we only vary  $\delta$  during the new fit, while keeping other iHOD parameters unchanged from the constraints listed in the table 2 of Paper I. The new best-fitting  $\delta$  is 0.44 (0.42 in Paper I). The new best-fitting halo quenching parameters are  $\{\lg M_h^{qc}, \mu^c, \lg M_h^{qs}, \mu^s\} = \{11.78, 0.41, 12.19, 0.24\}$ , slightly different from Paper II (c.f., table 2).

Conceptually, iHOD mock galaxies can be generated from simulated halo catalogues by drawing  $M_*$  and  $b_{g-r}$  jointly from  $P(M_*, b_{g-r} | M_h)$ , which can be trivially derived from  $P(M_h | M_*, b_{g-r})$  using Bayes’ Theorem. But since the centrals and satellites follow distinct stellar-to-halo mass relations, in practice it is more convenient to assign stellar masses to the centrals and satellites separately, then label them red or blue, and at last give them positions and velocities. We describe the three steps in turn below.

- The first step is to assign stellar masses. Using the best-fitting iHOD parameters as input, we derive the mean SHMR and its logarithmic scatter for central galaxies (c.f., Fig. 10 of Paper I), and the conditional stellar mass functions (CSMF) for satellites in halos of different masses ( $\phi(M_*^{\text{sat}} | M_h)$ ; c.f., Fig. 12 of Paper I). For each simulated halo with mass  $M_h$ , we randomly draw the stellar mass of its central galaxy from the log-normal distribution  $P(M_*^{\text{cen}} | M_h)$  specified by the combination of SHMR and its logarithmic scatter at  $M_h$ ; we then assign it a set of satellite galaxies, whose stellar mass distribution follows  $\phi(M_*^{\text{sat}} | M_h)$ .

- Secondly, for each central (satellite) galaxy residing in a halo of  $M_h$ , we label it red or blue according to the mean red central (satellite) galaxy fraction at that halo mass (i.e., Equations 2 and 3), predicted by the best-fitting halo quenching parameters. The label indicates whether the galaxy colour is above or below  $(g-r)_{\text{split}}$ , but without a particular  $g-r$  value.

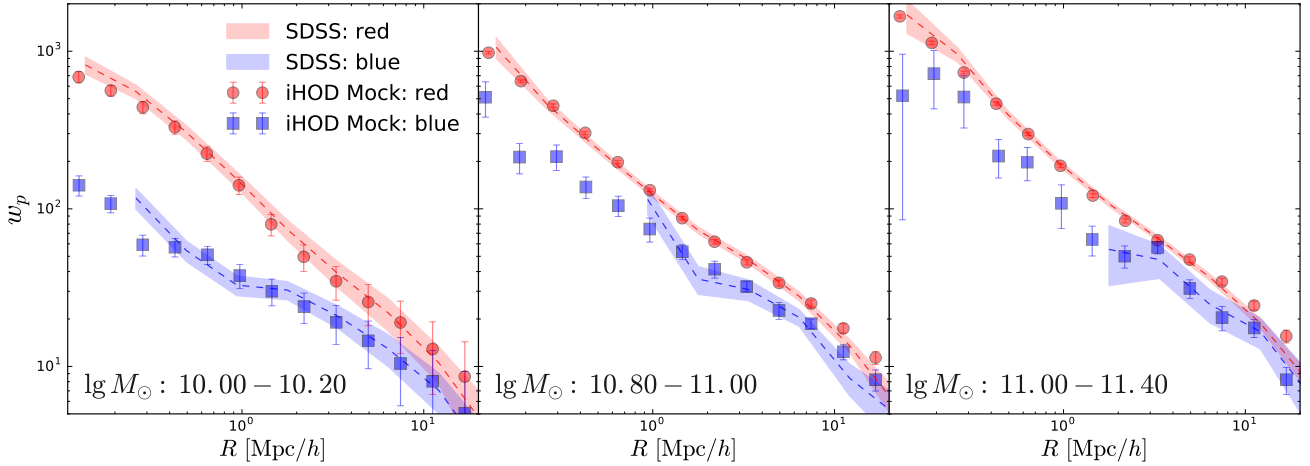


**Figure 1.** Comparison between the projected auto-correlation functions  $w_p(R)$  measured from the SDSS main sample (dashed curves with shaded uncertainty bands) and predicted by the iHOD mock galaxy catalogues with halo quenching (data points with errorbars), for red and blue galaxies within three different stellar mass bins ( $\lg M_*$  range listed in the bottom left of each panel), respectively. The low (left panel) stellar mass mock sample is derived from Bolshoi, while the high (right panel) and intermediate (middle panel) stellar mass samples are from MDR1. The blue bands are cut off on small scales because the SDSS blue galaxies becomes increasingly rare at higher  $M_*$ .

- We predict the relative positions and velocities of mock galaxies with respect to the halo center as follows. For each main halo with concentration  $c$ , radius  $r_{200m}$ , and 3D dark matter velocity dispersion  $\sigma$ , the central galaxy is placed at the center, while the satellite positions are assigned randomly according to an isotropic NFW profile with  $c_g \equiv f_c \times c$  and a cut-off at  $r_{200m}$ . The galaxy velocities are assigned based on the galaxy velocity bias model described in Guo et al. (2015), where the relative velocities of central and satellite galaxies follow Gaussian distributions with zero means and standard deviations of  $\sigma_c = \alpha_c \sigma$  and  $\sigma_s = \alpha_s \sigma$ , with  $\alpha_c = 0.20$  and  $\alpha_s = 1.00$ , respectively. Note that we do not fit the observed monopole and quadrupole of the correlation functions for the values of  $\alpha_s$  and  $\alpha_c$ , as was done in Guo et al. (2015), because our analyses focus on projected quantities and the impact of peculiar velocities on those quantities is minimal.

It is worth nothing that by adopting a halo boundary of  $r_{200m}$ , we have implicitly assumed that the halo quenching effects have a sharp transition across  $r_{200m}$  without extending beyond individual halos in those mocks, which is not necessarily an unreasonable assumption (Baxter et al. 2017). We have also ignored the radial segregation of satellite stellar mass (Adami et al. 1998; Presotto et al. 2012; Roberts et al. 2015; Contini & Kang 2015; Kafle et al. 2016; van den Bosch et al. 2016; Nascimento et al. 2017) and colour (Chen 2008; Prescott et al. 2011; Woo et al. 2013; Wang et al. 2014; Woo et al. 2017) in this study. Whether a true 2-halo environmental dependence or galactic conformity would emerge on scales beyond  $3 h^{-1} \text{Mpc}$  is independent of the choice for the halo quenching boundary or the segregation effects, as they would only modify the shape of the mark correlation functions and conformity signals in the 1-halo regime.

As a sanity check, Figure 1 compares the projected correlation functions  $w_p$  measured from the SDSS (dashed

curves with shaded uncertainty bands) and the iHOD mock galaxy samples (data points with errorbars), for red and blue galaxies within three different stellar mass bins. Clearly, the mock galaxy samples provide an excellent description of the spatial clustering of the red and blue galaxies in SDSS. In addition, the g-g lensing signals (not shown here, but see Fig. 8 in Paper II) predicted by the red and blue mock galaxies also agree with that measured from SDSS very well. Taking advantage of the realistic red galaxies in the mock catalogue, Zu et al. (2016) constructed a mock cluster catalogue that mimics the clustering of the redMaPPer clusters (Rykoff et al. 2014) and predicted the observed level of cluster assembly bias in SDSS.

We emphasize that it is imperative for the red and blue mock galaxies to accurately reproduce the observed auto-correlation ( $w_p$ ) and cross-correlation with the dark matter ( $\Delta\Sigma$ ), as demonstrated by Figure 1. For any mock galaxy catalogues that fail to recover  $w_p$  and  $\Delta\Sigma$ , systematics discrepancies in these two observables could potentially propagate into the systematic uncertainties of the mark correlation functions and the red galaxy fractions around isolated primaries, rendering the physical interpretation of those measurements inconclusive.

### 3 ASSIGNING GALAXY COLOURS

The simple halo quenching model described above allows us to label each mock galaxy as red or blue, i.e., to predict whether the  $g-r$  colour of that galaxy is above or below  $(g-r)_{\text{split}}$ . Although this binary split is adequate for the purpose of distinguishing different quenching models in Paper II, it is insufficient for studying the environmental dependence of colours, which are sensitive to the small yet spatially coherent variations of galaxy colours. Therefore, we need to

further assign specific  $g-r$  values to the mock galaxies before comparing them to the data.

Most importantly, we need to make sure that the colour distribution of mock galaxies at any given stellar mass,  $P(g-r|M_*)$ , is consistent with SDSS. [Kauffmann \(2015\)](#) found a significant discrepancy between the conformity observed in SDSS and that predicted by a cosmological hydrodynamic simulation (*Illustris*; [Vogelsberger et al. 2014](#); [Bray et al. 2016](#)); But since the detailed SFR and colour distributions within *Illustris* are quite different from those in the observations, it is unclear whether the existing physical processes in the simulation should be capable of reproducing the correct large-scale conformity, or some key environmental quenching mechanism is missing. In this analysis, we aim to eliminate this ambiguity by drawing conclusions based on mock galaxies that are generated with different quenching physics but have the identical  $P(g-r|M_*)$  as the real galaxies.

In this section, we will derive  $P(g-r|M_*)$  by fitting double-Gaussian PDFs to SDSS colour distributions in § 3.1, and comment on the origin of scatter in galaxy colours in § 3.2. We next describe the three colour assignment schemes in turn in § 3.3 and examine the theoretical sources of conformity in those schemes in § 3.4.

### 3.1 Modelling the Bimodal Distributions of Colour

To accurately measure the underlying colour distributions in SDSS, we select a suite of volume-limited stellar mass-binned samples, with equal bin width of 0.1 dex starting at  $\lg M_* = 10.0$ . The stellar mass limit adopted in this study is the same as the ‘‘mixture limit’’  $M_*^{\text{mix}}(z)$  defined in Paper I,

$$\lg M_*^{\text{mix}}(z) = 5.4 \times (z - 0.025)^{0.33} + 8.0, \quad (4)$$

corresponding to the characteristic stellar mass at which the average galaxy colour  $\langle g-r \rangle$  sharply transitions from below to above 0.8 at any given  $z$ . As explained in Paper I, galaxy samples selected above this limit can be regarded as being approximately volume-complete. As a result, we measure the colour distributions from the suite of stellar-mass binned samples, and use them directly as the input data for fitting  $P(g-r|M_*)$ .

Following previous studies of colour bimodality ([Skibba & Sheth 2009](#); [Taylor et al. 2015](#); [Paranjape et al. 2015](#)), we employ the double-Gaussian function as the analytic form of  $P(g-r|M_*)$ ,

$$P(g-r|M_*) = f'_{\text{red}}(M_*) \mathcal{N}^{\text{red}} + [1 - f'_{\text{red}}(M_*)] \mathcal{N}^{\text{blue}}, \quad (5)$$

where  $\mathcal{N}^{\text{red}}$  and  $\mathcal{N}^{\text{blue}}$  represent the red and blue Gaussian components, respectively, while  $f'_{\text{red}}(M_*)$  is the fraction of the red Gaussian component. Note that  $f'_{\text{red}}(M_*)$  is an unknown free parameter in the double-Gaussian model, different from the usual red galaxy fraction

$$f_{\text{red}}(M_*) = \int_{(g-r)_{\text{split}}|M_*}^{+\infty} P(g-r|M_*) d(g-r), \quad (6)$$

which can be directly measured from SDSS. During the fitting, we not only minimize the  $\chi^2$  between the double-Gaussian and the colour distribution measured from each volume-limited sample, but also ensure that the predicted

$f_{\text{red}}$  is equal to the measured value from SDSS. We impose the latter primarily for the sake of consistency between the colour assignments below and the halo quenching model described in § 2, which is based on the division of red vs. blue galaxies using  $(g-r)_{\text{split}}$ .

Figure 2 compares the best-fitting double-Gaussians (gray curves) with the colour distributions (black histograms) measured from eight selected stellar mass samples, with the stellar mass range, redshift range, and the red galaxy fraction of each sample indicated on the top left of every panel. The red solid and blue dashed distributions indicate the red and blue Gaussian components, and the orange dotted vertical lines indicate the red vs. blue division defined by  $(g-r)_{\text{split}}$ . In general, the best-fitting models of  $P(g-r|M_*)$  provide an adequate description of the observed colour distributions across all measured stellar mass bins, showing only very minor discrepancies in the so-called ‘‘green valley’’ where the two components overlap.

Figure 3 summarizes the result of the fitting. In the top panel, the red solid and blue dotted lines indicate the means of the red and blue Gaussian components, respectively, while each colour-shaded band represents the scatter about the respective mean. The orange dashed line indicates  $(g-r)_{\text{split}}$ , the red vs. blue division used for defining  $f_{\text{red}}$ . Clearly, there is progressively more overlap between the two Gaussian components at higher mass, mainly due to the two means approaching each other. As a result, there is a discrepancy of  $\sim 0.10$  between  $f_{\text{red}}$  and  $f'_{\text{red}}$  above  $\lg M_* = 10$ , as shown by the two curves in the bottom panel. The strong overlap makes it difficult to distinguish the true quiescent vs. active galaxies based on colour at the high-mass end (discussed further later).

We will assign galaxy colours in two steps. In the first step, we generate an ensemble of mock colours at each  $M_*$  (adopting a bin size of  $\Delta \lg M_* = 0.1$ ) by drawing random  $g-r$  values from the best-fitting analytic  $P(g-r|M_*)$ . Within each narrow stellar mass bin, we divide those mock colours into red and blue, so that the colours of red galaxies follow

$$P^{\text{red}}(g-r|M_*) = \begin{cases} \frac{P(g-r|M_*)}{f_{\text{red}}(M_*)} & \text{if } g-r \geq (g-r)_{\text{split}} \\ 0 & \text{if } g-r < (g-r)_{\text{split}}, \end{cases} \quad (7)$$

while the colours of blue galaxies follow

$$P^{\text{blue}}(g-r|M_*) = \begin{cases} \frac{P(g-r|M_*)}{1-f_{\text{red}}(M_*)} & \text{if } g-r < (g-r)_{\text{split}} \\ 0 & \text{if } g-r \geq (g-r)_{\text{split}}. \end{cases} \quad (8)$$

We then distribute those red (blue) colours among the red (blue) galaxies based on three different schemes below. In this way, a red (blue) galaxy will retain its red (blue) label across the three catalogues, but obtain a different red (blue)  $g-r$  colour depending on the relative strength of halo quenching vs. galaxy assembly bias assumed in each catalogue.

### 3.2 Origin of Scatter in the Colour-Stellar Mass Relations

In essence, our goal is to find out which halo properties are the most responsible for driving the intrinsic scatter in the colour-stellar mass relation (CSMR) of red or blue galaxies. Below  $10^{11} h^{-2} M_{\odot}$ , the scatter in the red/blue galaxy CSMR at any given  $M_*$  is dominated by that of the intrinsic

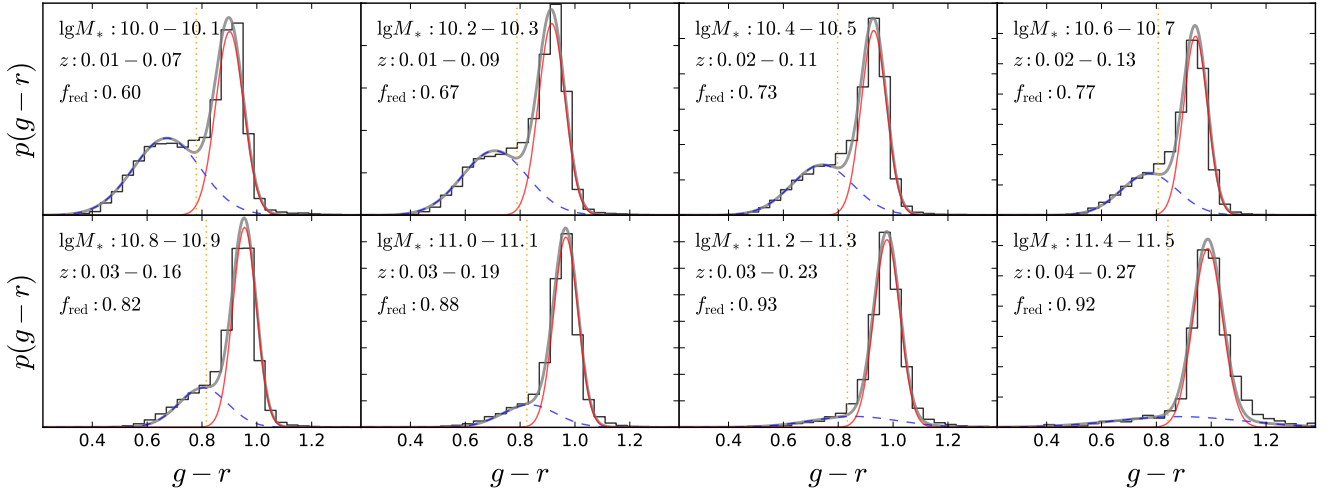


**Figure 2.** Illustration of the  $g-r$  colour distributions in eight different stellar mass bins. In each panel, the black histogram is directly measured from a volume-limited SDSS galaxy sample ( $\lg M_*$  and  $z$  ranges of each sample listed in the top left). The gray distribution is the best-fitting mixture model that consists of two Gaussian components (red solid and blue dashed). The orange dotted vertical line indicates the  $M_*$ -dependent colour cut used for dividing the galaxies into red and blue populations, with the fraction of red galaxies  $f_{\text{red}}$  listed in the legend.

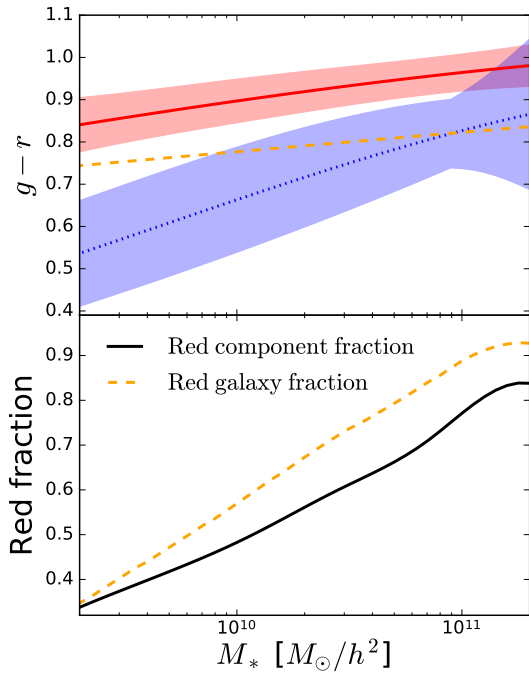


**Figure 3.** *Top panel:* The derived colour-stellar mass relations of the red and blue Gaussian components. The red solid curve and the width of the red shaded band indicate the mean and the dispersion of the red component, while the blue dotted curve and shaded band are the blue component. The orange dashed line is the colour division we use to separate galaxies into red and blue populations (Equation 1). *Bottom panel:* The black solid curve is the fraction of the red Gaussian component as a function of  $M_*$ , using the normalization of the red Gaussian component at each  $M_*$ ; the orange dashed curve is the fraction of the red galaxies as a function of  $M_*$ , using the orange dashed line in the top panel to split galaxies into red and blue.

stellar colours of galaxies, which reflects the diversity in the integrated star-formation histories of those red/blue galaxies at that stellar mass. Starting from  $\lg M_*=11$ , however, there is a sudden increase in the scatter of the blue component, as shown by the blue shaded band in the top panel of Figure 3. This increase is unlikely intrinsic, but caused by a combination of strong dust reddening in some edge-on spirals and starbursts triggered by major mergers. The internal dust reddening in spirals only becomes prominent at the high mass end, probably because they have accumulated significant dust during past star formation activities and are physically large with long path lengths through the edge-on discs (Masters et al. 2010).

Ideally, we would prefer using the intrinsic stellar colours that are corrected for internal dust. Taylor et al. (2015) tried to estimate the internal dust reddening empirically from the internal extinctions ( $A_V$ ) given by Stellar Population Synthesis fits (assuming the extinction law of Calzetti et al. 2000). After subtracting this estimated reddening, they found substantial decrease in the dispersion of the blue component at high  $M_*$ , mostly due to the large corrections to dusty star-forming systems. However, it is quite difficult to assess the systematic uncertainties associated with the assumed dust properties, especially the propensity to over-correct systems with little or no dust (Taylor et al. 2015). Therefore, for the sake of simplicity, we will not apply any reddening correction on the  $g-r$  colours in this analysis, and assume that the extrinsic scatter can be effectively accounted for by reducing the cross-correlation between the observed colour and halo properties. For galaxies with  $M_* > 10^{11} h^{-2} M_\odot$ , the cross-correlation is further diluted by the extra extrinsic scatter and the severe overlap between the red and blue components.

### 3.3 Colour Assignment Schemes

With the mock colours generated from  $p^{\text{red}}$  and  $p^{\text{blue}}$ , we now proceed to construct three more comprehensive halo quenching mock catalogues for our analysis in § 4.

#### 3.3.1 Baseline Halo Quenching

The *baseline* halo quenching mock catalogue corresponds to our null hypothesis — the scatter within either colour population is independent of halo properties, despite the fact that the blue-to-red transformation is statistically driven by halo mass. In this case, the relative colour of a red galaxy with respect to the RS ridge-line is independent of its host halo properties, and the galaxies redder than the ridge-line (hereafter referred to as the  $\mathcal{R}^+$  galaxies) would live in similar halos as the less red galaxies (hereafter referred to as  $\mathcal{R}^-$ ). Likewise in the blue population, the bluer half ( $\mathcal{B}^+$ ) would mix well with the less blue half ( $\mathcal{B}^-$ ) in terms of their dark matter habitats. To build such a catalogue, we simply assign the red  $g-r$  colours randomly to the red mock galaxies by drawing from Equation (7) (similar to the ‘AbM’ model in Saito et al. 2016), and likewise for the blue colours for blue galaxies using Equation (8). This baseline halo quenching mock should exhibit the minimum level of the environmental dependence of colours and colour conformity around centrals among all the halo quenching mocks.

#### 3.3.2 Fiducial Halo Quenching

Within the halo quenching model, there are at least two channels through which the environmental dependence of colours could be boosted beyond the baseline mock. One possibility is that halo mass remains the key quantity in “tinting” the colour of a red or blue galaxy, so that the  $\mathcal{B}^+$ ,  $\mathcal{B}^-$ ,  $\mathcal{R}^-$ , and  $\mathcal{R}^+$  galaxies at fixed  $M_*$  live in progressively more massive halos. This naturally extends the simple halo quenching model from modelling binary to continuous colour variables. To build such an extension, we introduce the cross-correlation coefficients between colour and halo mass at fixed stellar mass,  $\rho_m^{\text{cen}}$  and  $\rho_m^{\text{sat}}$ , as our two new parameters. As the red fraction of central galaxies is a steeper function of halo mass than that of satellites, we choose a higher value for  $\rho_m^{\text{cen}}$  (0.5) than  $\rho_m^{\text{sat}}$  (0.3) for galaxies with  $\lg M_* < 11$ ; For the reasons outlined in § 3.2, at  $\lg M_* \geq 11$  we reduce the value of  $\rho_m^{\text{sat}}$  to zero, while keeping the value of  $\rho_m^{\text{cen}}$  at 0.5 — we assume that the increase in the extrinsic scatter of colour is mainly due to the enhanced activity level of satellites in massive halos. We hereafter adopt this catalogue as our *fiducial* halo quenching mock.

#### 3.3.3 “Assembly-Biased” Halo Quenching

Alternatively, galaxy assembly bias could coherently modulate the quenching processes within the same large-scale environment, making galaxies slightly redder (bluer) in over (under)-dense regions than in the field. If such galaxy assembly bias effect is mediated via some secondary halo property other than  $M_h$ , we would expect a strong correlation between galaxy colour and that mediator. For example, one might speculate that the older halos host slightly redder galaxies than the younger ones at the same mass, if

they have had more time forming and quenching galaxies in denser environments. However, the theoretical connection between any secondary halo properties and galaxy formation remains obscure. But for the purpose of our study, it is not necessary to distinguish which halo property is the true underlying mediator, as long as it is a good indicator for halo assembly bias that strongly correlates with large-scale overdensity.

Halo assembly bias reveals itself as the dependence of halo clustering on a variety of secondary halo properties, the three most prominent of which are concentration, age, and spin (Sheth & Tormen 2004; Wechsler et al. 2006; Gao & White 2007; Lee et al. 2017). Among the three, the age dependence is much weaker than the other two on the high mass end (Jing et al. 2007), while the impact of halo spin on galaxy formation is likely the most complicated (van den Bosch et al. 2002; Lacerna & Padilla 2012; Dubois et al. 2014; Teklu et al. 2015), depending on spin-tidal field alignment (Aragón-Calvo et al. 2007; Zhang et al. 2009; Libeskind et al. 2013; Shi et al. 2015; Kang & Wang 2015) and halo merger history (D’Onghia & Navarro 2007; Welker et al. 2014; Bett & Frenk 2016; Rodríguez-Gomez et al. 2016). Therefore, we will focus on halo concentration as our proxy for galaxy assembly bias.

To remove the anti-correlation between halo concentration and mass (Wechsler et al. 2006), we define a new variant of the concentration parameter for each halo with mass  $M_h$ ,

$$\ln c_{\text{assem}} = \begin{cases} \ln c - \langle \ln c(M_h) \rangle & \text{if } M_h \leq M^{\text{nl}} \\ -(\ln c - \langle \ln c(M_h) \rangle) & \text{if } M_h > M^{\text{nl}} \end{cases}, \quad (9)$$

where  $c$  is the standard halo concentration parameter,  $\langle \ln c(M_h) \rangle$  is the average logarithmic concentration of all halos at  $M_h$ , and  $M^{\text{nl}}$  is the characteristic non-linear mass scale ( $\lg M^{\text{nl}} = 12.8$  in our mocks). Since halo concentration follows a log-normal distribution at fixed halo mass, and the logarithmic scatter is roughly constant with halo mass, there is little residual correlation between  $c_{\text{assem}}$  and  $M_h$ . In addition, we flip the sign inside the parentheses at  $M^{\text{nl}}$ , because the cross-correlation coefficient between halo concentration and overdensity goes from being positive to negative across  $M^{\text{nl}}$  (Gao & White 2007; Jing et al. 2007). Therefore, this new parameter  $c_{\text{assem}}$  serves as our proxy for halo assembly bias, and is positively correlated with large-scale overdensity on all mass scales.

Similar to the fiducial halo quenching mock, we introduce two new parameters,  $\rho_c^{\text{cen}}$  and  $\rho_c^{\text{sat}}$ , as the cross-correlation coefficients between colour and  $c_{\text{assem}}$  for the centrals and satellites, respectively. For our *assembly-biased* halo quenching catalogue, we set both cross-correlation coefficients to be unity, thereby maximizing the level of conformity that can be achieved by turning on galaxy assembly bias within halo quenching.

We emphasize that our assembly-biased halo quenching mock is fundamentally different from a pure assembly-bias quenching mock like, e.g., the age-matching mock of Hearin et al. (2014). At fixed  $M_*$ , in the assembly-biased halo quenching mock, the blue-to-red transition is statistically determined by the simple halo quenching model of Paper II, while the more vs. less red (blue) colours are driven by their halo assembly bias via  $c_{\text{assem}}$ ; In the age-matching mock, however, the colour of a galaxy at fixed  $M_*$  depends almost exclusively on its halo assembly bias via a characteristic red-



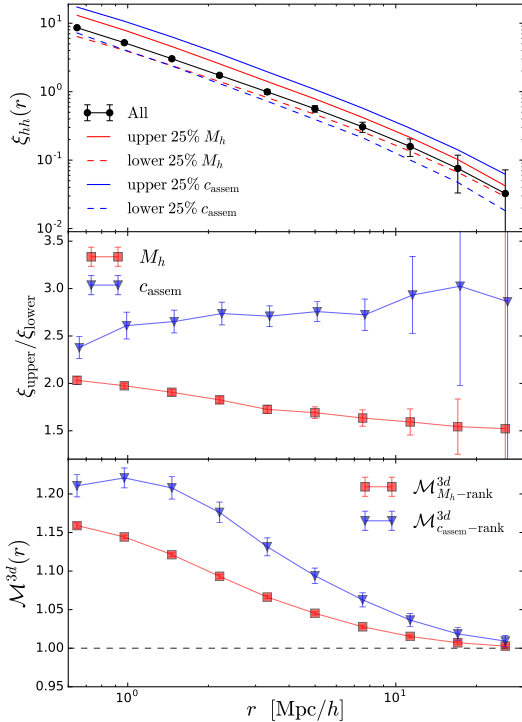


**Figure 4.** *Top panel:* 3D real-space correlation functions ( $\xi_{hh}$ ) of dark matter halos in the **BoLshoi** simulation. Black circles with errorbars show the measurement for all halos with  $M_h > 10^{11} h^{-1} M_\odot$ . Red solid and dashed curves are the  $\xi_{hh}$  for halos in the upper and lower 25 per cent tails of the  $M_h$  distribution, while the blue solid and dashed curves indicate the upper and lower quartiles of  $c_{\text{assem}}$ . As defined by Equation 9,  $c_{\text{assem}}$  is a proxy for the halo assembly bias effect, and the clustering difference between the two  $c_{\text{assem}}$  quartiles is thus solely driven by halo assembly bias, independent of any halo-mass-related trends (see text for details). *Middle panel:* Ratios between the  $\xi_{hh}$  of halos in the upper and lower quartiles of  $M_h$  (red squares) and  $c_{\text{assem}}$  (blue triangles), respectively. *Bottom panel:* Mark correlation functions of halos with  $M_h > 10^{11} h^{-1} M_\odot$ , using  $M_h$ -rank (red squares) and  $c_{\text{assem}}$ -rank (blue triangles) as marks, respectively.

shift  $z_{\text{starve}}$ . For most of the centrals (below  $10^{11} h^{-2} M_\odot$ ),  $z_{\text{starve}}$  is equivalent to the formation redshift of the subhalos, but at very high  $M_*$  it largely corresponds to the first epoch at which halo mass exceeds  $10^{12} h^{-1} M_\odot$ .

### 3.4 Theoretical Sources of Conformity in Mock Catalogues

Before delving into our main results in the next section, we explore the two theoretical sources of conformity in our three halo quenching mock catalogues in Figure 4. In the top panel, we show the 3D real-space correlation functions ( $\xi_{hh}$ ) of all **BoLshoi** halos above  $10^{11} h^{-1} M_\odot$  (black circles), along with that of halos in the upper (solid) and lower (dashed) quartiles of the distributions in  $M_h$  (red) and  $c_{\text{assem}}$  (blue). The middle panel shows the ratios between the  $\xi_{hh}$  of two halo subsamples selected by  $M_h$  (red squares) and  $c_{\text{assem}}$  (blue triangles), respectively. As expected from the standard theory of halo biasing (Sheth & Tormen 1999),

the high mass halos have a stronger clustering strength than the low mass ones on all scales, while the halo assembly bias effect is illustrated by the high vs. low- $c_{\text{assem}}$  halos — the clustering biases of these two halo subsamples are different despite having the same average mass ( $\langle \lg M_h \rangle \approx 11.45$ ). However, the bias ratios here do not give us full information on the potential conformity signal that can be induced by  $M_h$  or  $c_{\text{assem}}$ .

On the contrary, the mark correlation function is an ideal tool for revealing the environmental dependence of halo/galaxy properties. The 3D real-space mark correlation is measured as

$$\mathcal{M}^{3d}(r) = \frac{WW}{DD} = \frac{1 + W(r)}{1 + \xi(r)}, \quad (10)$$

where  $WW$  and  $DD$  are the mark-weighted and unweighted number counts of pairs with 3D distance  $r$  (Sheth et al. 2005; Skibba et al. 2006), while  $W(r)$  and  $\xi(r)$  are the mark-weighted and unweighted real-space correlation functions, respectively. Since the marks are normalized to have a mean of unity, if the distribution of marks is independent of environment,  $\mathcal{M}^{3d}(r)$  should be unity on all scales due to the lack of conformity. Otherwise, if the marks of two objects are correlated over some scale,  $\mathcal{M}^{3d}(r)$  will deviate above unity at that scale.

The bottom panel of Figure 4 shows the 3D real-space mark correlation functions of halos, using the rank-orders of  $M_h$  (red squares) and  $c_{\text{assem}}$  (blue triangles) as marks. We use rank-orders so that the distributions of the two marks are the same uniform distribution from 0 to 2, making a direct comparison between the two mark correlations feasible (Skibba et al. 2013). Both mark correlation signals decline with radius, but stay significantly above unity on scales up to  $15 h^{-1} \text{Mpc}$ , exhibiting strong conformities in the 2-halo regime. Therefore, we expect that an environmental dependence of colours (including a 2-halo colour conformity) would naturally arise in all three halo quenching mocks, but the overall amplitude and scale-dependence would be different from one to another, due to the varying relative strength of the mass effect and assembly bias in each mock.

Finally, we emphasize that the underlying drivers of the environmental effects in galaxy colours are different among the three mocks — while the baseline and the fiducial halo quenching mocks rely solely on the environmental dependence of the halo mass function to produce an “indirect” environmental effect, the assembly-biased halo quenching mock predicts both direct and indirect environmental effects, via the halo assembly bias effect of  $c_{\text{assem}}$  and the environmental dependence of halo mass functions, respectively. Meanwhile, the age-matching mock employs the halo assembly bias effect of  $z_{\text{starve}}$  to produce direct environmental effects in the spatial distribution of galaxy colours.

## 4 RESULTS

In this Section, we present the main results of our analysis, by comparing the three halo quenching mock catalogues with the SDSS data using different measurements. These include the clustering  $w_p$  and weak lensing  $\Delta\Sigma$  of the  $\mathcal{R}^+$  and  $\mathcal{R}^-$  galaxies, the 2D mark correlation functions of colours  $M_{g-r}$ , and the red galaxy fractions around red vs. blue primaries  $f_{\text{red}}(R)$ .

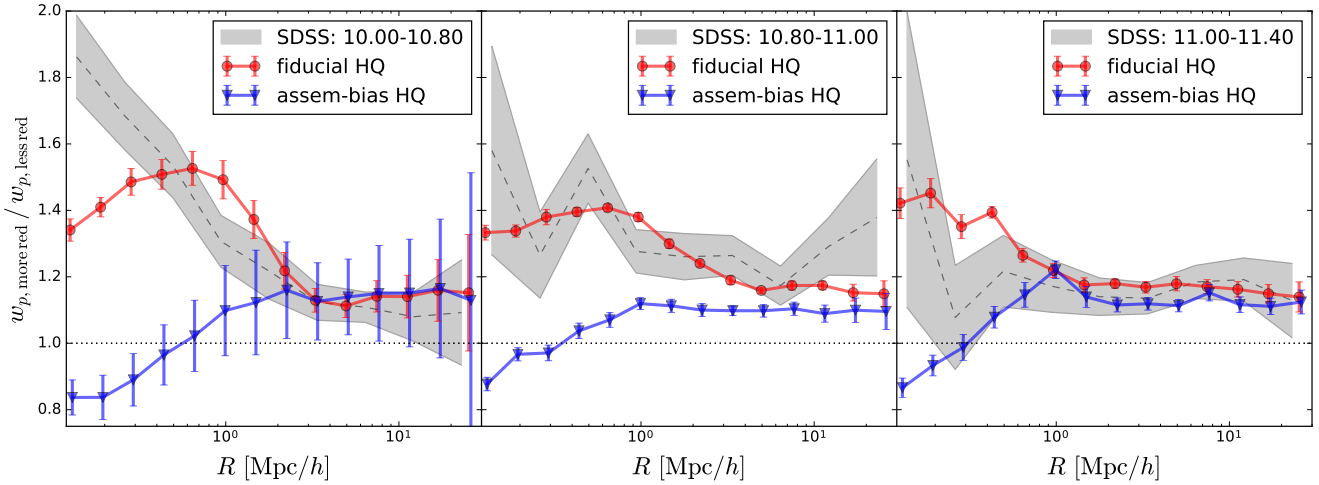


**Figure 5.** Ratio between the projected cross-correlation functions  $w_p$  of more red vs. less red galaxies (both cross-correlated with the parent red galaxy sample) within three different stellar mass bins. In each panel, the dashed curve with the gray uncertainty band is measured from a volume-limited sample in SDSS, while red circles and blue triangles are predictions from our fiducial halo quenching mock and a modified halo quenching model with assembly-bias effects, respectively.

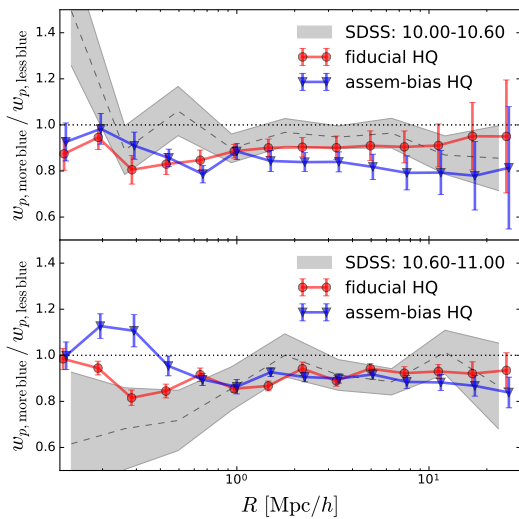


**Figure 6.** Similar to Figure 5 but for more blue vs. less blue galaxies within two different stellar mass bins.

#### 4.1 Clustering and Lensing of “More Red” vs. “Less Red” Galaxies

As a sanity check, we will first compare the clustering and  $g$ - $g$  lensing of the  $\mathcal{R}^+$  (more red) and  $\mathcal{R}^-$  (less red) galaxies predicted by the mocks to that measured from data. By construction, the three halo quenching mocks assign different values of red  $g-r$  colours to the red galaxies that share the same set of halos in the simulation, therefore placing the  $\mathcal{R}^+$  and  $\mathcal{R}^-$  galaxies into different halos. In particular, the  $\mathcal{R}^+$  and  $\mathcal{R}^-$  galaxies occupy halos with similar  $M_h$  and  $c_{\text{assem}}$  in the baseline mock, but live in halos of different  $M_h$  or  $c_{\text{assem}}$  in the other two mocks. This segregation of galaxies by halo properties, which is lacking in the baseline mock, dictates that the  $\mathcal{R}^+$  and  $\mathcal{R}^-$  galaxies will exhibit different

clustering and weak lensing signals, a prediction that can be directly tested using the SDSS data.

Figure 5 shows the ratios of the projected correlation functions  $w_p$  between the  $\mathcal{R}^+$  and  $\mathcal{R}^-$  galaxies for three different stellar mass bins. To obtain a more stable measurements of the clustering ratios, we compute the cross-correlations of the two subsamples with the overall red galaxy sample in each bin, instead of the auto-correlations shown in Figure 1. In each panel, the gray dashed curve with shaded band is the measurement from volume-limited samples in SDSS, and the data points with errorbars are predictions by the fiducial (red circles) and assembly-biased (blue triangles) halo quenching mocks. Clearly, the baseline mock, which predicts a  $w_p$  ratio of unity on all scales (dotted horizontal line), is readily ruled out in all three stellar mass bins. The fiducial halo quenching mock shows the best overall agreement with the SDSS measurements on all scales between  $0.1$  and  $25 h^{-1}\text{Mpc}$ , whereas the assembly-biased halo quenching mock only provides an adequate description of the SDSS measurements on scales beyond  $2 h^{-1}\text{Mpc}$  (except for the intermediate mass bin where it fails to match the data on all scales). It is worth noting that some of the discrepancies between the mock predictions and the SDSS measurements on small scales are caused by the lack of colour segregation in the mocks (e.g., the rapid increase of observed ratios on scales below  $0.2 h^{-1}\text{Mpc}$  in SDSS).

The assembly-biased halo quenching mock predicts that the  $\mathcal{R}^+$  and  $\mathcal{R}^-$  galaxies live in halos of similar mass (mostly above  $M^{\text{nl}}$ ), hence the similar small-scale amplitude of  $w_p$ . Furthermore, it predicts that the  $\mathcal{R}^+$  satellite galaxies live in high- $c_{\text{assem}}$  halos, which mainly correspond to low- $c$  halos and a less concentrated satellite distribution within halos, causing the ratio to cross from above to below unity on scales  $\lesssim 0.5 h^{-1}\text{Mpc}$ . In the low ( $\lg M_* = [10.0, 10.8]$ ) and intermediate ( $\lg M_* = [10.8, 11.0]$ ) stellar mass bins, however, neither the decrease of the ratio on small scales nor the ratio inversion at  $0.5 h^{-1}\text{Mpc}$  is seen in the data, indicating

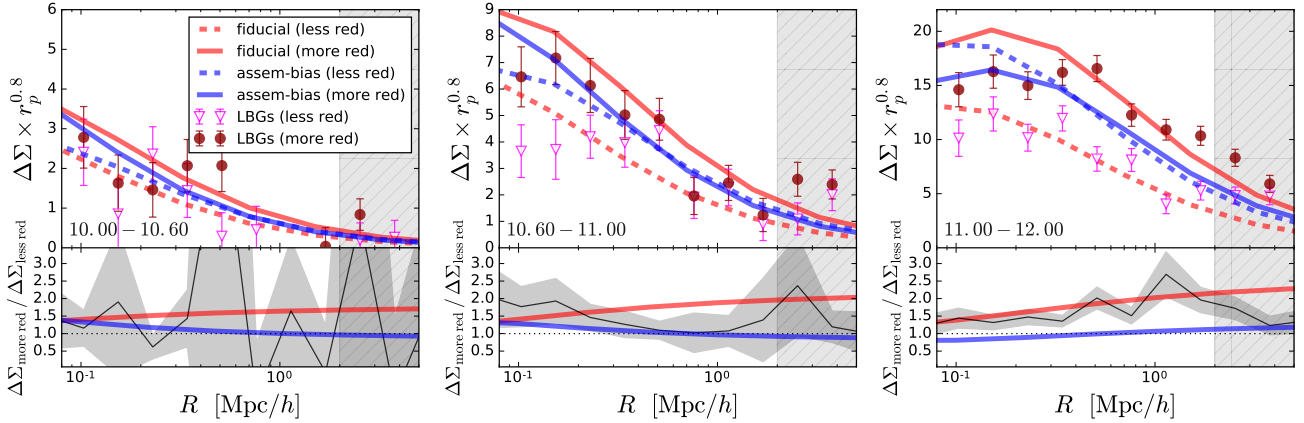


**Figure 7.** *Top panels:* Comparison between weak lensing signals measured from more red vs. less red locally brightest galaxy samples derived from SDSS (red filled circles and magenta open triangles with errorbars), and those predicted by our fiducial halo quenching mock (red solid and dashed curves) and an assembly-bias modified halo quenching mock (blue solid and dashed curves), for three different stellar mass bins. The model curves (predicted using only the 1-halo term) cannot be directly compared with data inside the gray vertical bands, which indicate the scales at which the 2-halo term becomes important. *Bottom panels:* Ratios between the  $\Delta\Sigma$  profiles of the more red vs. less red LBGs, as measured from weak lensing in SDSS (black curve with gray uncertainty bands), and predicted from the fiducial (red) and assembly-bias modified (blue) halo quenching models.

that the assembly-biased halo quenching is not an adequate model for the colouring of red-sequence *satellite* galaxies below  $10^{11} h^{-2} M_{\odot}$ . For the high mass bin ( $\lg M_* = [11.0, 11.4]$ ), the SDSS measurement is consistent with predictions from both mocks, in part due to the large errorbars resulting in poor discriminating power on the small scales where the predictions from those mocks differ.

Similarly, Figure 6 shows the ratio comparison between the more blue vs. less blue galaxies in two different stellar mass bins. Due to the lack of a distinct colour ridgeline in the blue portion of the colour-stellar mass diagram, we divide each blue sample into two halves using the median blue colour as a function of  $M_*$ . At any given stellar mass, the two subsamples of blue galaxies in SDSS exhibit weaker discrepancies in their clustering biases than the two red galaxy subsamples, and the observed clustering ratio is also better-reproduced by the blue galaxies in the fiducial mock than those in the assembly-biased halo quenching mock on all scales.

For diagnosing the colour properties of central galaxies, we turn to the weak lensing signals around central galaxies with different shades of red. Following Mandelbaum et al. (2016), we select a sample of “locally brightest galaxies” (LBGs; Planck Collaboration et al. 2013) from the SDSS spectroscopic sample as our candidates for central galaxies, and measure the weak lensing profiles for the red LBG subsamples split by the RS ridgeline at fixed stellar mass. Mandelbaum et al. (2016) discovered a strong bimodality in the average halo mass between the red and blue LBGs, which we subsequently interpreted as the indication of a dominant halo quenching mechanism using our iHOD framework in Paper II.

In the same spirit as Mandelbaum et al. (2016), we show the weak lensing profiles  $\Delta\Sigma$  of the  $\mathcal{R}^+$  (maroon filled circles) and  $\mathcal{R}^-$  (magenta open triangles) LBGs within three stellar mass bins in the upper panels of Figure 7. In each upper panel, we also show the predictions from the fiducial (red

solid and dashed curves) and assembly-biased (blue solid and dashed) halo quenching mocks. We ignore the profiles beyond  $R = 2h^{-1}\text{Mpc}$  (covered by the gray shaded region) as they do not carry clean information on the halo mass profile. In the lower panels, we show the ratios between the  $\mathcal{R}^+$  and  $\mathcal{R}^-$  weak lensing profiles for the SDSS LBGs (black curve with gray shaded bands), the fiducial halo quenching mock (red curve), and the assembly-biased halo quenching mock (blue curve). As expected, the assembly-biased halo quenching mock predicts a  $\Delta\Sigma$  ratio of roughly unity on all scales, modulo minor tilt due to differences in halo concentration. But in the fiducial mock, the  $\mathcal{R}^+$  central galaxies exhibit stronger weak lensing amplitude than the  $\mathcal{R}^-$  centrals on the relevant scales.

In the lowest mass bin ( $\lg M_* = [10.0, 10.6]$ ), both mock predictions are consistent with the data, but the large uncertainties in the weak lensing measurements prevent us from making any statistical statements on one mock being preferred by the data. Similarly in the intermediate mass bin ( $\lg M_* = [10.6, 11.0]$ ), both mock predictions are roughly consistent with the measured  $\Delta\Sigma$  profiles. However, the  $\Delta\Sigma$  ratio measurement on scales above  $0.6 h^{-1}\text{Mpc}$  slightly prefers the assembly biased halo quenching mock, but shows a strong discrepancy between the two subsamples on scales below  $0.6 h^{-1}\text{Mpc}$ , which tends to favor the fiducial halo quenching mock. Fortunately, the weak lensing measurements in the high mass bin ( $\lg M_* = [11.0, 12.0]$ ) leave no ambiguity as to which mock is the superior model for colouring high-mass central galaxies — the fiducial halo quenching mock provides an excellent description for the  $\Delta\Sigma$  profiles of the more vs. less red LBGs and the ratio between the two, while the assembly-biased halo quench mock completely fails to do so.

Combining Figures 5, 6, and 7, it is clear that the fiducial halo quenching mock significantly out-performs the other two mocks in describing the clustering and weak lensing of red galaxies split by the RS ridge-line. However, the

weak lensing measurements for low- $M_*$  galaxies have large uncertainties, and we cannot perform the same lensing test on the blue galaxies due to their low number density in this mass range. With this result and its limitations in mind, we will turn to the mark correlation functions of colours for a clearer picture in the next subsection.

#### 4.2 Environmental Dependence: Mark Correlation Functions of Galaxy Colours

Marked statistics are an efficient tool for quantifying the correlation between the properties (i.e., marks) of galaxies and their environment (Martínez et al. 2010). Here we focus on the 2D projected mark correlation function of  $g-r$  colours  $M_{g-r}(R)$  as our diagnostic of the underlying driver of environmental dependence of galaxy colours, whether it be halo mass, halo assembly bias, or some combination of the two.

Following earlier studies (Skibba et al. 2006; Skibba & Sheth 2009; Skibba et al. 2012) of galaxy mark correlation functions in SDSS, we define  $M_{g-r}(R)$  as

$$M_{g-r}(R) = \frac{1 + W_p(R)/R}{1 + w_p(R)/R}, \quad (11)$$

where  $W_p$  and  $w_p$  are the mark-weighted and unweighted projected correlation functions of galaxies, respectively. This particular definition makes  $M(R) \sim \mathcal{M}^{3d}(r \equiv 2R)$  on large scales, where  $w_p(R)/R \sim \xi$ .

We measure  $M_{g-r}(R)$  by combining the measurements of  $W_p$  and  $w_p$  as in Equation 11, and compute the uncertainties by Jackknife re-sampling 200 sub-regions within the sample footprint. We refer readers to Paper I for the technical details on the projected correlation function measurements. To make sure that the mark values are always positive, we adopt  $\exp(g-r)/\langle \exp(g-r) \rangle$  as the mark in both the data and mock catalogues. Since the mock colour distribution at each fixed  $M_*$  is almost identical to that in SDSS, we can compare the colour-mark correlation functions of the mock and data catalogues directly. More importantly, since all the mocks accurately reproduce the abundance, spatial clustering, and g-g lensing of the red and blue galaxies in SDSS, any discrepancy between the colour-mark correlations of the mock and the data galaxies would be a clean sign of incorrect colour assignment in that mock.

Figure 8 compares the colour-mark correlation functions between the data and various mocks within six different stellar mass bins. In each panel, the gray shaded band indicates the measurement ( $\pm 1\sigma$  range) from a volume-limited sample of SDSS galaxies within the  $\lg M_*$  range (listed on the top left); Orange squares with errorbars are measured from the baseline halo quenching mock, while the red and blue thick curves are from the fiducial and assembly-biased halo quenching mocks, respectively, with similar uncertainties (not shown) as in the baseline case. We also show the measurement (magenta triangles with errorbars) from the age-matching mock produced by Hearin et al. (2014)<sup>3</sup>, which serves as an interesting limiting case in which the galaxy assembly bias effect is maximized and the halo quenching effect is minimized. Overall, the observed mark

correlation signal decreases with increasing stellar mass, partly due to the lack of a prominent blue population in the high- $M_*$  samples. The observed  $M_{g-r}$  signal also decreases as a function of distance, analogous to the 1-halo to 2-halo transition in the regular correlation functions. However, in all the stellar mass bins below  $10^{11} h^{-2} M_\odot$ , the observed mark correlations stay significantly above unity on scales up to  $15 h^{-1} \text{Mpc}$ , indicating strong environmental dependence of galaxy colours at fixed  $M_*$ .

The colour-mark correlation functions predicted by the baseline halo quenching model (orange squares with error-bars) have similar shapes as the  $M_{g-r}$  measured from SDSS, but their overall amplitudes are 30-50% lower than the observed ones. The lower amplitudes are expected: by design the baseline model includes the least amount of halo quenching effect that is allowed by the measurements of the clustering and g-g lensing of red and blue galaxies in SDSS.

With a stronger coupling between halo mass and galaxy colour, the fiducial halo quenching mocks (red curves) are able to roughly reproduce the correct amplitudes of  $M_{g-r}$ , especially the deviation from unity on large scales. Similar to the baseline model, the fiducial halo quenching mock is consistent with the clustering and lensing measurements of the red and blue galaxies in SDSS. In addition, the fiducial model is also the only one among the three colour assignment schemes that is consistent with the observations of the clustering and lensing of the more vs. less red (blue) galaxies. Therefore, it is tempting based on the combined evidence so far to argue that the fiducial halo quenching mock roughly encodes the correct information on the connection between galaxy quenching and halo properties in SDSS. The primary discrepancy between the mark correlations predicted by the fiducial model and the data is that the mock curves have a slightly sharper transition from 1-halo to 2-halo scales compared to the data, probably due to the lack of colour segregation and the sharp halo boundaries adopted in the mock. It is worth noting that the 1-halo to 2-halo transition is notoriously difficult to model correctly even for regular correlation functions (not marked).

The assembly-biased halo quenching mock predicts a very similar amplitude of  $M_{g-r}$  on large scales as the fiducial mock and the data, and is thus consistent with the SDSS measurements. However, recall that the assembly-biased model represents the maximum amount of galaxy assembly bias (mediated by concentration) that can be allowed in the halo quenching scenario — the colour of a red/blue galaxies is maximally coupled with the rank-order of  $c_{\text{assem}}$ , our proxy for the halo environment; therefore, it is very unlikely that halo concentration is the underlying driver for the “tinting” of red or blue galaxies under the halo quenching framework. On small scales, the predicted curves level off and approach unity for the three stellar mass bins above  $\lg M_* = 10.6$ . Similar to the small-scale behavior seen in Figure 5 (blue curves), the low amplitudes on scales below  $0.3 h^{-1} \text{kpc}$  are caused by the lower values of  $g-r$  colours assigned to the satellites in massive halos with high concentrations than those inside low-concentration clusters.

Unlike the three halo quenching mocks, the age-matching mock relies on galaxy assembly bias, i.e., by matching galaxy colours to their halo formation times at fixed  $M_*$ , to introduce the environmental dependence of galaxy colours. Clearly, the maximal coupling between

<sup>3</sup> [http://logrus.uchicago.edu/~aphearin/SDSS\\_Mock\\_Catalog/SDSS\\_Mock\\_Catalog.html](http://logrus.uchicago.edu/~aphearin/SDSS_Mock_Catalog/SDSS_Mock_Catalog.html)

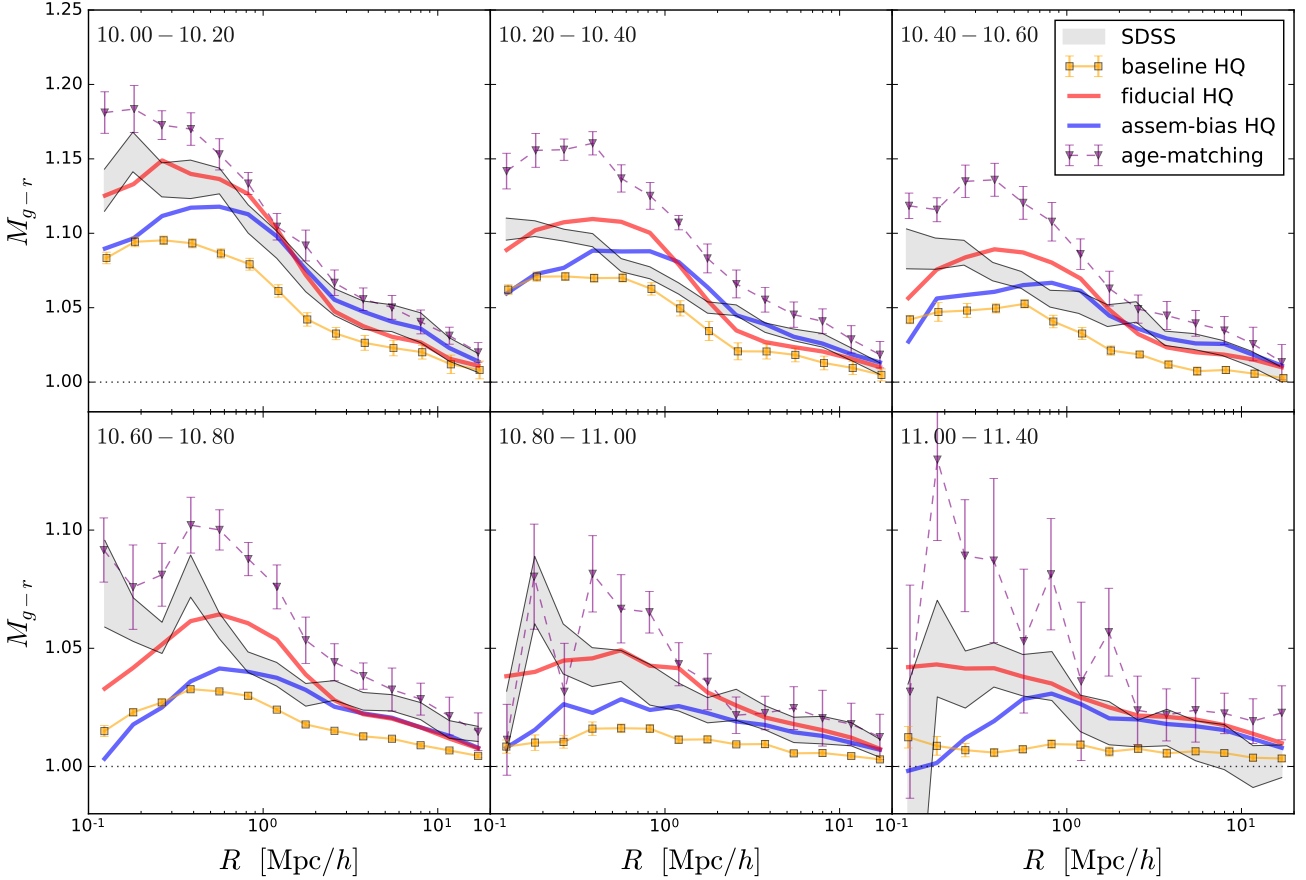


**Figure 8.** Mark correlation functions of galaxy  $g-r$  colours within six different stellar mass bins. In each panel, the gray uncertainty band indicates the mark correlation measured from a volume-limited galaxy sample in SDSS. Orange squares with errorbars show the prediction from the baseline halo quenching mock, while red and blue curves are predictions from the fiducial and assembly-bias modified halo quenching mocks. The sizes of errorbars (not shown here) on the red and blue curves are comparable to that in the baseline model. Purple triangles with errorbars are predicted from an age-matching mock with strong assembly bias effect on colours (Hearin et al. 2014). Among the four models, the fiducial halo quenching mock provides the best overall description for the scale and stellar mass dependence of colours in SDSS.

galaxy colour and halo age is strongly disfavored by the data, as the predicted mark correlation functions (magenta triangles with errorbars) are 40-50% higher than the observations on almost all scales and for four of the six stellar mass bins. A more reasonable fit to the data can be potentially achieved by tuning down the coupling strength between galaxy colour and halo age, but as we pointed out in Sec. 1, without halo quenching it is still unlikely to reproduce the observed bimodality in the host halo mass of red vs. blue central galaxies. We need to globally match not just the mark correlation functions, but also the regular two-point correlations, for which Paper I and II demonstrated halo quenching is necessary.

Clearly, Figure 8 shows that there is significant environmental dependence of galaxy colours up to scales as large as  $15 h^{-1} \text{Mpc}$ , and the fiducial halo quenching model is able to reproduce this large-scale environmental dependence of colours across the entire stellar mass range we probed ( $> 10^{10} h^{-2} M_{\odot}$ ). However, a strong environmental effect revealed by the mark correlation functions does not necessarily translate to a strong colour conformity, which is

exclusively a phenomenon surrounding central galaxies. In particular, the mark correlation function has two contributing sources: one is the galactic conformity between the central galaxies and neighbouring galaxies (i.e., the **cen-cen** and **cen-sat** terms), and the other is the correlation between the colours of satellites (i.e., the **sat-sat** term). Therefore, it is possible that the **sat-sat** contribution could dominate the signal in the mark correlation functions, while the conformity contribution stays confined within the 1-halo regime. If proven true, this scenario would explain the findings by Hearin et al. (2015), that an HOD model of galaxy colours cannot induce 2-halo conformity, despite of the strong environmental effect in the spatial distribution of galaxy colours.

Figure 9 compares the three contributions, **cen-cen** (magenta solid), **cen-sat** (orange dotted), **sat-sat** (blue dashed), between the fiducial halo quenching (upper panels) and the age-matching (lower panels) mocks in three stellar mass bins (columns from left to right: [10.2, 10.4], [10.6, 10.8], [10.8, 11.0]). In each panel we also show the overall mark correlation functions measured in the

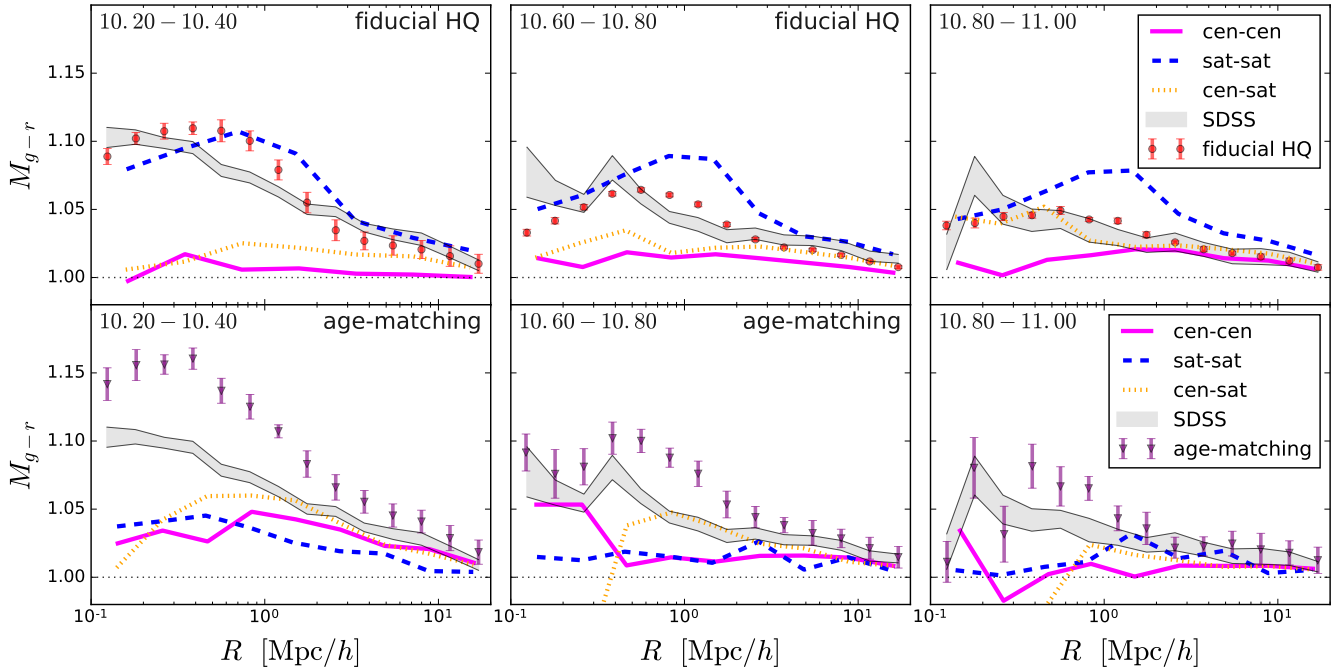


**Figure 9.** Mark correlation functions of **cen-cen** (solid magenta), **cen-sat** (dotted orange), and **sat-sat** (dashed blue) pairs, predicted by the fiducial halo quenching (upper panels) and the age-matching (lower panels) mocks for three different stellar mass bins. In each panel, we also show the prediction for the overall mark correlation function (symbols with errorbars) and the SDSS measurement (gray shaded band). The combination of the **cen-cen** and **cen-sat** components indicates the level of conformity in each model.

mock (symbols with errorbars) and the data (gray shaded bands) from Figure 8.

In the low- $M_*$  bin (left column), the environmental dependence of colours in the fiducial halo quenching mock (upper left) is primarily driven by the correlation between the satellite colours, and partly by the colour conformity between central galaxies and satellites. In halo quenching, the dominant **sat-sat** term is caused by the strong halo quenching effect on the satellites of rich groups and clusters, which tend to live in dense environments; The **cen-cen** term is very weak, as in this low stellar mass regime the red vs. blue central galaxies are living in halos whose masses differ only by a factor of two or less, due to the weak halo quenching effect below  $10^{12} h^{-1} M_\odot$ . On the contrary, the age-quenching mock (lower left) predicts strong **cen-cen** and **cen-sat** terms, because the host halos of those centrals (with  $M_h < M^{nl}$ ) exhibit a strong assembly bias effect (Gao et al. 2005); The **sat-sat** term is substantially weaker than the conformity terms, due to the weaker halo assembly bias effect in their massive host halos (with  $M_h > M^{nl}$ ).

At higher stellar masses (middle and right columns), the **sat-sat** term remains dominant in the upper panels (halo quenching), but the **cen-cen** term begin to increase, indicating stronger conformity effects for higher  $M_*$  primaries in the halo quenching scenario. For the age-matching model, the **cen-cen** term decreases at higher  $M_*$ , because the halo assembly bias effect becomes weaker with increasing  $M_h$  (Jing et al. 2007).

From Figure 9, we can see that the environmental dependence of colours shown in the halo quenching mocks are

largely driven by the correlation between the colours of satellites. This finding explains the lack of large-scale conformity in the HOD model of colours in Hearin et al. (2015) — a strong mark correlation function signal does not necessarily imply strong conformity on large scales, especially for galaxies with  $\lg M_* < 10.4$ . However, the 2-halo conformity signal predicted by our fiducial halo quenching mock increases rapidly with stellar mass, becoming comparable to the age-matching prediction at  $\lg M_* \sim 10.6$ , and much stronger than age-matching at  $\lg M_* > 10.8$ . Furthermore, it is worth nothing that even in the lowest stellar mass bin probed here ( $\lg M_* \sim 10.2$ ), there still exists some colour conformity signal on large scales, mostly due to the correlation between the colours of central galaxies and that of satellites inside nearby massive halos. In the next subsection, we will explore whether such a level of 2-halo conformity is consistent with the observed red galaxy fractions around red vs. blue primaries in SDSS.

### 4.3 Conformity: Red Galaxy Fraction Around Red vs. Blue Isolated Primaries

So far, the fiducial halo quenching mock has successfully passed the sanity check in § 4.1 and reproduced the observed strong environmental dependence of colours in § 4.2. As we alluded to in Section 1, Tinker et al. (2017) and Sin et al. (2017) showed that the observed level of large-scale conformity is very sensitive to the isolation criteria for identifying primary galaxies. They found significant reduction in the conformity signal around low-mass primary galaxies after re-

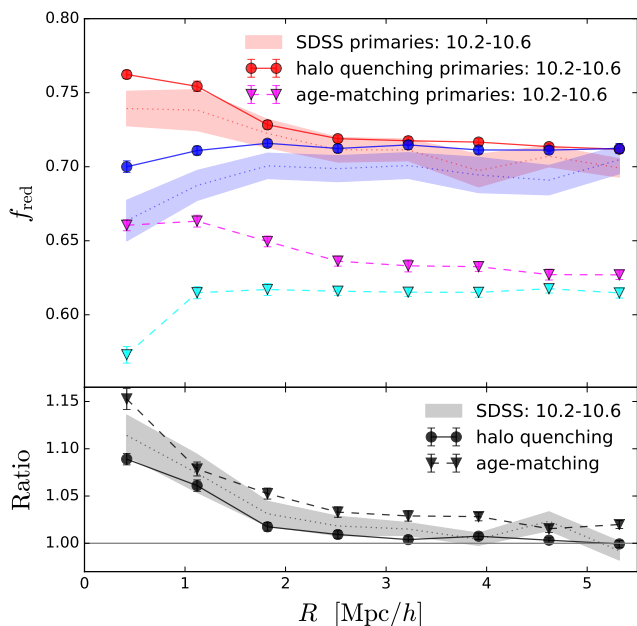


**Figure 10.** Red galaxy fractions as functions of projected distance from red vs. blue isolated primaries with  $\lg M_* = [10.2 - 10.6]$ . In the top panel, dotted curves with red and blue uncertainty bands are the measurements from a volume-limited sample in SDSS. The red and blue circles with errorbars are the predictions from our fiducial halo quenching mock, while the magenta and cyan triangles are from the age-matching mock (the lower average  $f_{\text{red}}$  in the age-matching results is due to sample incompleteness in the mock). The bottom panels show the ratios between the red fraction profiles of the red vs. blue isolated primaries, for SDSS galaxies (gray bands), our fiducial halo quenching mock (circles), and the age-matching mock (triangles). The deviations of ratio profiles from unity indicate colour conformity.

moving a small fraction of mis-identified primaries, which are revealed by the group finders (Yang et al. 2007; Tinker et al. 2011) to be living inside or near massive systems (e.g., the Coma cluster). However, based on the iterative reshift-space friends-of-friends technique, the group finders also have their own limitations in crowded environments (Campbell et al. 2015). Since our goal here is to find out whether the level of conformity predicted by the mocks is consistent with observations, the conclusion should not depend on the criteria for finding centrals, as long as we self-consistently apply the same criteria to the mock and data catalogues. Therefore, we will adopt the simple isolation criteria of Kauffmann et al. (2013), and directly measure the red galaxy fractions around the red and blue isolated primaries in SDSS, without resorting to more stringent criteria based on complicated group finders.

For the candidate sample for primary galaxies, we choose the log-stellar mass range of  $[10.2, 10.6]$ , similar to the main stellar mass range probed in Kauffmann et al. (2013) and Hearin et al. (2015). For the secondary galaxy sample, we select all galaxies with stellar mass above  $5 \times 10^9 h^{-2} M_\odot$ , 0.5 dex below the minimum stellar mass of the primaries. We adopt the same criteria in Kauffmann et al. (2013) to find the isolated primaries — a galaxy with stel-

lar mass  $M_*$  is defined as an isolated primary if there is no other galaxy with stellar mass greater than  $M_*/2$  within a projected radius of  $350 h^{-1} \text{kpc}$  and with velocity difference less than  $500 \text{ km s}^{-1}$ .

We apply the same sample selection and isolation criteria in the fiducial halo quenching and the age-matching mock catalogues, and the purities (i.e., fraction of true central galaxies among the selected isolated primaries) are 0.81 (fiducial) and 0.95 (age-matching), respectively. The lower purity in the iHOD mock is largely due to the higher average frequency of having a satellite galaxy that is at least twice as massive as the central within halos above  $10^{13} h^{-1} M_\odot$  (see the lower panels of Fig. 5 in Paper II). Since the age-matching mock catalogue is incomplete below  $\lg M_* \sim 10$ , we expect the mean red galaxy fraction to be different from the observations, but the conformity signal, i.e., the ratio between the red fractions around red vs. blue primaries, should be preserved. For the observations, we also applied the same isolation criteria to a volume-limited SDSS galaxy sample with  $M_*$  above  $5 \times 10^9 h^{-2} M_\odot$  and a redshift range of  $[0.01, 0.055]$ . We then measure the red galaxy fractions as functions of projected distance away from the red and blue primaries, as well as the ratio between the red galaxy fractions around red vs. blue primaries in each catalogue.

Figure 10 compares the conformity signals measured from the fiducial halo quenching mock (circles), the age-matching mock (triangles), and the SDSS galaxies (shaded bands), respectively. All the errorbars are  $1\text{-}\sigma$  uncertainties derived from jackknife re-sampling, and the sizes of the errorbars measured from the two mock catalogues are comparable to the size of the symbols. The top panel shows  $f_{\text{red}}(R)$ , the red galaxy fractions as functions of projected distance away from the isolated primaries. The amplitude and scale-dependence of  $f_{\text{red}}(R)$  predicted by the fiducial halo quenching mock agree very well with the observations. This agreement is not by construction, because the iHOD quenching parameters were constrained solely from the clustering and g-g lensing information, without any input from the relative abundance of red/blue galaxies. The age-matching predictions for the overall red galaxy fractions are substantially lower, likely due to the sample incompleteness below  $10^{10} h^{-2} M_\odot$ . However, the age-matching mock clearly predicts strong conformity, i.e., large discrepancy between the red galaxy fractions around red vs. blue primaries, while the level of conformity in the data and the fiducial halo quenching mock is weaker.

The bottom panel of Figure 10 presents a clearer picture of conformity via the ratio between the red galaxy fractions around red vs. blue primaries. The SDSS galaxies show substantial colour conformity signal on projected distances up to  $2\text{-}3 h^{-1} \text{Mpc}$ , beyond which the signal becomes consistent with having no conformity on scales  $\sim 5 h^{-1} \text{Mpc}$ . The ratio predicted by the age-matching model is slightly higher than the measurement, and stays significantly above 1.0 on all scales. As expected, the ratio predicted by the fiducial halo quenching mock is lower than that predicted by the age-matching mock on all scales, due to the weaker cen-cen contribution to the environmental dependence of colours. However, the halo quenching prediction is in good agreement with the SDSS measurement, showing considerable conformity on scales below  $3 h^{-1} \text{Mpc}$ .

Figure 10 demonstrates that the level of conformity observed at stellar mass around a few  $\times 10^{10} h^{-2} M_{\odot}$  can be naturally explained by the HOD model of galaxy colours that includes a halo quenching prescription for assignment of colours. Inside the halo quenching mock, the conformity signal is primarily (81%) sourced by the correlation between the colours of central galaxies and their neighbouring galaxies, and partly (19%) induced by the mis-identified primaries that are satellites of the more massive halos. The underlying drivers of both components, however, are the same combination of the environmental dependence of halo mass function and the strong dependence of galaxy quenching on halo mass — an indirect environmental effect imprinted on galaxy formation.

## 5 SUMMARY AND DISCUSSION

### 5.1 Fiducial Picture of Halo Quenching

In this paper, we have investigated whether halo mass quenching is capable of reproducing the environmental dependence of galaxy colours and the large-scale galactic conformity observed in SDSS, for which recent studies suggested that a strong galaxy assembly bias effect may be required. Developed in the first two papers of the series (Zu & Mandelbaum 2015, 2016), the best-fitting iHOD halo quenching model can accurately describe the observed abundance, spatial clustering, and weak gravitational lensing of the red and blue galaxies in SDSS, serving as an ideal test-bed for exploring the environmental effects predicted by halo quenching. For the prediction, we start by producing quiescent and active mock galaxies within a suite of  $N$ -body cosmological simulations based on the best-fitting iHOD halo quenching prescription, which describes the red galaxy fractions of the centrals and satellites as powered-exponential functions of the halo mass. We then assign  $g-r$  colours to the quiescent and active galaxies separately at fixed stellar mass  $M_*$ , by introducing correlations between galaxy colours and the mass of their dark matter halos. In our fiducial halo quenching model, we set the cross-correlation coefficients  $\rho_m^{\text{cen}}$  between halo mass and the red or blue central galaxies to be 0.5, while assuming a weaker coupling with halo mass for the red and blue satellites ( $\rho_m^{\text{cen}} = 0.3$  below  $10^{11} h^{-2} M_{\odot}$  and 0.0 above).

Despite the fact that the quantity that determines the galaxy colours in the halo quenching model is associated with individual halos, the fiducial halo quenching mock predicts strong environmental dependence of galaxy colours — the mark correlation functions of colours deviate significantly above unity on scales up to  $15 h^{-1} \text{Mpc}$  in all stellar mass bins, in excellent agreement with the measurements from SDSS. This strong environmental dependence is induced by the combination of halo quenching and the environmental dependence of the halo mass function: in denser environments there are more massive halos, hence more quenched and redder galaxies at fixed  $M_*$ . By decomposing the predicted colour-mark correlation function at fixed  $M_*$  into **cen-cen**, **cen-sat**, and **sat-sat** components, we find that the overall environmental dependence is dominated by the **sat-sat** term. However, there still remains a significant level of **cen-cen** and **cen-sat** contributions, i.e., galactic conformity, on scales up to  $15 h^{-1} \text{Mpc}$ .

After applying the same isolation criteria of Kauffmann et al. (2013) to the halo quenching mock, we demonstrate that the halo quenching model correctly reproduces the level of large-scale conformity in SDSS, as measured by the red galaxy fractions around the red vs. blue primary galaxies. Confirming the results from Tinker et al. (2017) and Sin et al. (2017), we find that  $\sim 19\%$  of the primaries in the mock are mis-identified satellite galaxies, which contribute a significant false conformity signal to the red fraction of distant neighbours.

To summarize, the fiducial halo quenching model provides a remarkably simple yet accurate picture of the spatial distribution of galaxy colors in the local Universe ( $z < 0.25$ ), including the colour dependence of galaxy clustering and weak gravitational lensing, the mark correlation functions of colours, and the large-scale galactic conformity in SDSS. On the contrary, models that rely on the halo assembly bias effect to quench star formations have great difficulties in matching to those observations, whether it be the age-matching model of Hearin et al. or the assembly-biased halo quenching model developed in our analysis.

### 5.2 Alternative Environmental Effects as a Test of Halo Quenching

There are at least two aspects of the large-scale environment that one could imagine might affect halo and galaxy properties: one is the large-scale background density, and the other is the large-scale tidal tensor field, i.e., the geometrical environment. In this paper we are primarily concerned with the former, but there could be additional dependences of quenching on the geometrical environment, which can be classified as clusters, filaments, sheets and voids via the Hessian matrix of the gravitational potential (Hahn et al. 2007; Forero-Romero et al. 2009; Hoffman et al. 2012). Alonso et al. (2015) investigated the variation of halo mass functions in different geometrical environments and found that at fixed large-scale overdensity, the halo mass functions are similar among the four different types of structures within the cosmic web. Therefore, under the fiducial picture of halo quenching there should be no colour dependence on the geometrical type of the environment.

However, some halo properties, like the halo spin and shape, depend strongly on the tidal and velocity shear fields (Hahn et al. 2007), and it is plausible that they could also affect galaxy quenching. Observationally, there is tentative evidence for correlations between galaxy properties (colour, size, spin, morphology, bar strength, etc) and the proximity to various geometrical environments (Pandey & Bharadwaj 2006; Zhang et al. 2013, 2015; Chen et al. 2017). Therefore, it will be interesting to predict the distributions of galaxy colours in different geometrical environments from the fiducial halo quenching mock, and compare to the measurements from data. Any discrepancies would signal additional environmental effects that cannot be accounted for by the halo quenching model, or any galaxy formation models that are insensitive to the tidal tensor field.

### 5.3 Theoretical Implications and Future Outlook

Under our fiducial halo quenching picture, the efficiency of galaxy quenching is tied to the strength of the gravita-



tional potential in the host halos, which could drive virial shocks that heat up the gas and/or harbor AGNs that inhibit star formation via powerful feedback processes. The great success of this simple picture, combined with the lack of any discernible galaxy assembly bias effect, suggests that galaxy quenching is likely a local process, in the sense that it is largely determined by the physical conditions inside a halo. In particular, the termination of star formation becomes prevalent when the halo reaches a critical mass of  $M_h^{\text{crit}} \sim 10^{12} h^{-1} M_\odot$ . This value of  $M_h^{\text{crit}}$ , derived from the observational constraints in Paper II and in this paper under a different cosmology, is roughly the same for central and satellite galaxies, and is naturally expected from canonical halo quenching theory (Birnboim & Dekel 2003; Dekel & Birnboim 2006; Cattaneo et al. 2006). This scenario of galaxy quenching being locally driven by host halos is also consistent with the lack of environmental dependence in the mass-metallicity relation (MZR) of galaxies (Wu et al. 2017), while a strong correlation between quenching and halo formation time would instead shift the overall amplitude of the MZR with the large-scale overdensity.

The ability of our fiducial halo quenching model to capture the observed environmental dependence of colours is encouraging news to the modelling of large-scale structure in ongoing and upcoming surveys. In particular, the construction of large mock galaxy catalogues with realistic stellar mass and colour properties is vital to the success of future surveys like the Dark Energy Spectroscopic Instrument (DESI; DESI Collaboration et al. 2016), Prime Focus Spectrograph (PFS; Takada et al. 2014), and Large Synoptic Survey Telescope (LSST; LSST Science Collaboration et al. 2009), for validating analysis pipelines and extracting cosmological information (see also Smith et al. 2017). For example, the iHOD mock galaxy catalogue is one of the primary synthetic sky catalogues that are deployed within the web-based mock catalog validation and comparison framework for the LSST Dark Energy Science Collaboration (DESCQA; Heitmann et al. *in prep*). Furthermore, the success of the halo quenching model reinforces the theoretical foundation for the red-sequence based cluster finding algorithms in modern photometric surveys (Rykoff et al. 2014) — the richness of a cluster  $\lambda$ , defined by  $\lambda(M_h) \equiv f_{\text{red}}(M_h) \times N_{\text{sat}}(M_h)$ , is more tightly correlated with  $M_h$  than either  $f_{\text{red}}$  or  $N_{\text{sat}}$  individually, and is insensitive to the average age of its subhalos or the large-scale environment.

Another exciting prospect is to apply the iHOD halo quenching framework to high redshifts. In particular, the Bright Galaxy Survey (BGS) program within DESI will conduct a magnitude-limited survey of approximately 10 million galaxies with a median redshift of 0.2. When combined with the current analysis of the SDSS main spectroscopic sample, the iHOD modelling of the BGS galaxies will enable an exquisite understanding of the evolution of galaxy quenching properties over the past  $\sim 2$  Gyrs, which is comparable to the observed star formation efficiency timescale of the molecular gas (Leroy et al. 2008), as well as the expected timescale for quenching (Wetzel et al. 2013; Hahn et al. 2016). At slightly higher redshifts ( $z \sim 0.5$ ), a comprehensive iHOD modelling will also shed important insight on the apparent inconsistency between the clustering and lensing of galaxies under the Planck15 cosmology (Planck Collaboration et al. 2015; Leauthaud et al. 2016).

Finally, this paper concludes our three-paper series by building the fiducial halo quenching mock catalogue that accurately reproduces the spatial clustering, weak lensing, and density environment of galaxies at any given stellar mass and colour within the local Universe. We will be happy to provide our mock catalogues or generate new mock catalogues with user-defined halo catalogues for those interested, upon request.

## ACKNOWLEDGEMENTS

We thank Ravi Sheth and David Weinberg for helpful discussions. YZ and RM acknowledge the support by the U.S. Department of Energy (DOE) Early Career Program. YZ is also supported by a CCAPP fellowship. The authors gratefully acknowledge the Gauss Centre for Supercomputing e.V. (www.gauss-centre.eu) and the Partnership for Advanced Supercomputing in Europe (PRACE, www.prace-ri.eu) for funding the MultiDark simulation project by providing computing time on the GCS Supercomputer SuperMUC at Leibniz Supercomputing Centre (LRZ, www.lrz.de). The Bolshoi simulations have been performed within the Bolshoi project of the University of California High-Performance AstroComputing Center (UC-HiPACC) and were run at the NASA Ames Research Center.

## REFERENCES

- Adami C., Biviano A., Mazure A., 1998, *A&A*, **331**, 439  
 Alonso D., Eardley E., Peacock J. A., 2015, *MNRAS*, **447**, 2683  
 Ann H. B., Park C., Choi Y.-Y., 2008, *MNRAS*, **389**, 86  
 Aragón-Calvo M. A., van de Weygaert R., Jones B. J. T., van der Hulst J. M., 2007, *ApJ*, **655**, L5  
 Bahé Y. M., McCarthy I. G., Balogh M. L., Font A. S., 2013, *MNRAS*, **430**, 3017  
 Bardeen J. M., Bond J. R., Kaiser N., Szalay A. S., 1986, *ApJ*, **304**, 15  
 Baxter E., et al., 2017, preprint, ([arXiv:1702.01722](https://arxiv.org/abs/1702.01722))  
 Behroozi P. S., Wechsler R. H., Wu H.-Y., 2013, *ApJ*, **762**, 109  
 Bekki K., Couch W. J., Shioya Y., 2002, *ApJ*, **577**, 651  
 Berlind A. A., Weinberg D. H., 2002, *ApJ*, **575**, 587  
 Berti A. M., Coil A. L., Behroozi P. S., Eisenstein D. J., Bray A. D., Cool R. J., Moustakas J., 2017, *ApJ*, **834**, 87  
 Bett P. E., Frenk C. S., 2016, *MNRAS*, **461**, 1338  
 Birnboim Y., Dekel A., 2003, *MNRAS*, **345**, 349  
 Bond J. R., Cole S., Efstathiou G., Kaiser N., 1991, *ApJ*, **379**, 440  
 Bray A. D., et al., 2016, *MNRAS*, **455**, 185  
 Calzetti D., Armus L., Bohlin R. C., Kinney A. L., Koornneef J., Storchi-Bergmann T., 2000, *ApJ*, **533**, 682  
 Campbell D., van den Bosch F. C., Hearin A., Padmanabhan N., Berlind A., Mo H. J., Tinker J., Yang X., 2015, *MNRAS*, **452**, 444  
 Cattaneo A., Dekel A., Devriendt J., Guiderdoni B., Blaizot J., 2006, *MNRAS*, **370**, 1651  
 Chen J., 2008, *A&A*, **484**, 347  
 Chen Y.-C., et al., 2017, *MNRAS*, **466**, 1880  
 Cheung E., et al., 2016, *Nature*, **533**, 504  
 Contini E., Kang X., 2015, *MNRAS*, **453**, L53  
 Cooray A., Sheth R., 2002, *Phys. Rep.*, **372**, 1  
 Croton D. J., et al., 2006, *MNRAS*, **365**, 11  
 Croton D. J., Gao L., White S. D. M., 2007, *MNRAS*, **374**, 1303  
 DESI Collaboration et al., 2016, preprint, ([arXiv:1611.00036](https://arxiv.org/abs/1611.00036))  
 D’Onghia E., Navarro J. F., 2007, *MNRAS*, **380**, L58

- Dekel A., Birnboim Y., 2006, *MNRAS*, **368**, 2
- Di Matteo T., Springel V., Hernquist L., 2005, *Nature*, **433**, 604
- Dressler A., 1980, *ApJ*, **236**, 351
- Dubois Y., et al., 2014, *MNRAS*, **444**, 1453
- Fabian A. C., 2012, *ARA&A*, **50**, 455
- Font A. S., et al., 2008, *MNRAS*, **389**, 1619
- Forero-Romero J. E., Hoffman Y., Gottlöber S., Klypin A., Yepes G., 2009, *MNRAS*, **396**, 1815
- Gabor J. M., Davé R., 2015, *MNRAS*, **447**, 374
- Gao L., White S. D. M., 2007, *MNRAS*, **377**, L5
- Gao L., Springel V., White S. D. M., 2005, *MNRAS*, **363**, L66
- Gunn J. E., Gott III J. R., 1972, *ApJ*, **176**, 1
- Guo Q., et al., 2011, *MNRAS*, **413**, 101
- Guo H., et al., 2015, *MNRAS*, **453**, 4368
- Guzik J., Seljak U., 2002, *MNRAS*, **335**, 311
- Hahn O., Carollo C. M., Porciani C., Dekel A., 2007, *MNRAS*, **381**, 41
- Hahn C., Tinker J. L., Wetzel A. R., 2016, preprint, ([arXiv:1609.04398](https://arxiv.org/abs/1609.04398))
- Hartley W. G., Conselice C. J., Mortlock A., Foucaud S., Simpson C., 2015, *MNRAS*, **451**, 1613
- Hearin A. P., Watson D. F., 2013, *MNRAS*, **435**, 1313
- Hearin A. P., Watson D. F., Becker M. R., Reyes R., Berlind A. A., Zentner A. R., 2014, *MNRAS*, **444**, 729
- Hearin A. P., Watson D. F., van den Bosch F. C., 2015, *MNRAS*, **452**, 1958
- Hearin A. P., Zentner A. R., van den Bosch F. C., Campbell D., Tollerud E., 2016, *MNRAS*, **460**, 2552
- Hoffman Y., Metuki O., Yepes G., Gottlöber S., Forero-Romero J. E., Libeskind N. I., Knebe A., 2012, *MNRAS*, **425**, 2049
- Hopkins P. F., Hernquist L., Cox T. J., Di Matteo T., Martini P., Robertson B., Springel V., 2005, *ApJ*, **630**, 705
- Jing Y. P., Mo H. J., Börner G., 1998, *ApJ*, **494**, 1
- Jing Y. P., Suto Y., Mo H. J., 2007, *ApJ*, **657**, 664
- Kaffe P. R., et al., 2016, *MNRAS*, **463**, 4194
- Kang X., Wang P., 2015, *ApJ*, **813**, 6
- Kauffmann G., 2015, *MNRAS*, **454**, 1840
- Kauffmann G., Li C., Heckman T. M., 2010, *MNRAS*, **409**, 491
- Kauffmann G., Li C., Zhang W., Weinmann S., 2013, *MNRAS*, **430**, 1447
- Kawinwanichakij L., et al., 2016, *ApJ*, **817**, 9
- Kereš D., Katz N., Fardal M., Davé R., Weinberg D. H., 2009, *MNRAS*, **395**, 160
- Klypin A. A., Trujillo-Gomez S., Primack J., 2011, *ApJ*, **740**, 102
- Knobel C., Lilly S. J., Woo J., Kovač K., 2015, *ApJ*, **800**, 24
- Komatsu E., et al., 2009, *ApJS*, **180**, 330
- LSST Science Collaboration et al., 2009, preprint, ([arXiv:0912.0201](https://arxiv.org/abs/0912.0201))
- Lacerna I., Padilla N., 2012, *MNRAS*, **426**, L26
- Lacey C., Cole S., 1993, *MNRAS*, **262**, 627
- Leauthaud A., et al., 2012, *ApJ*, **744**, 159
- Leauthaud A., et al., 2016, preprint, ([arXiv:1611.08606](https://arxiv.org/abs/1611.08606))
- Lee C. T., Primack J. R., Behroozi P., Rodríguez-Puebla A., Hellinger D., Dekel A., 2017, *MNRAS*, **466**, 3834
- Lemson G., Kauffmann G., 1999, *MNRAS*, **302**, 111
- Leroy A. K., Walter F., Brinks E., Bigiel F., de Blok W. J. G., Madore B., Thornley M. D., 2008, *AJ*, **136**, 2782
- Li C., White S. D. M., 2009, *MNRAS*, **398**, 2177
- Libeskind N. I., Hoffman Y., Forero-Romero J., Gottlöber S., Knebe A., Steinmetz M., Klypin A., 2013, *MNRAS*, **428**, 2489
- Lin Y.-T., Mandelbaum R., Huang Y.-H., Huang H.-J., Dalal N., Diemer B., Jian H.-Y., Kravtsov A., 2016, *ApJ*, **819**, 119
- Ma C.-P., Fry J. N., 2000, *ApJ*, **543**, 503
- Mandelbaum R., Seljak U., Kauffmann G., Hirata C. M., Brinkmann J., 2006, *MNRAS*, **368**, 715
- Mandelbaum R., Wang W., Zu Y., White S., Henriques B., More S., 2016, *MNRAS*, **457**, 3200
- Martínez V. J., Arnalte-Mur P., Stoyan D., 2010, *A&A*, **513**, A22
- Martino M. C., Sheth R. K., 2009, *MNRAS*, **394**, 2109
- Masters K. L., et al., 2010, *MNRAS*, **404**, 792
- McCarthy I. G., Frenk C. S., Font A. S., Lacey C. G., Bower R. G., Mitchell N. L., Balogh M. L., Theuns T., 2008, *MNRAS*, **383**, 593
- Mo H. J., Mao S., 2002, *MNRAS*, **333**, 768
- Mo H. J., White S. D. M., 1996, *MNRAS*, **282**, 347
- More S., van den Bosch F. C., Cacciato M., Skibba R., Mo H. J., Yang X., 2011, *MNRAS*, **410**, 210
- Nascimento R. S., Ribeiro A. L. B., Lopes P. A. A., 2017, *MNRAS*, **464**, 183
- Ocvirk P., Pichon C., Teyssier R., 2008, *MNRAS*, **390**, 1326
- Oemler Jr. A., 1974, *ApJ*, **194**, 1
- Pahwa I., Paranjape A., 2016, preprint, ([arXiv:1612.00464](https://arxiv.org/abs/1612.00464))
- Pandey B., Bharadwaj S., 2006, *MNRAS*, **372**, 827
- Paranjape A., Kovač K., Hartley W. G., Pahwa I., 2015, *MNRAS*, **454**, 3030
- Peacock J. A., Smith R. E., 2000, *MNRAS*, **318**, 1144
- Planck Collaboration et al., 2013, *A&A*, **557**, A52
- Planck Collaboration et al., 2015, preprint, ([arXiv:1502.01589](https://arxiv.org/abs/1502.01589))
- Prada F., Klypin A. A., Cuesta A. J., Betancort-Rijo J. E., Primack J., 2012, *MNRAS*, **423**, 3018
- Prescott M., et al., 2011, *MNRAS*, **417**, 1374
- Presotto V., et al., 2012, *A&A*, **539**, A55
- Press W. H., Schechter P., 1974, *ApJ*, **187**, 425
- Roberts I. D., Parker L. C., Joshi G. D., Evans F. A., 2015, *MNRAS*, **448**, L1
- Rodríguez-Gomez V., et al., 2016, preprint, ([arXiv:1609.09498](https://arxiv.org/abs/1609.09498))
- Rodríguez-Puebla A., Primack J. R., Behroozi P., Faber S. M., 2016, *MNRAS*, **455**, 2592
- Rodríguez-Puebla A., Primack J. R., Avila-Reese V., Faber S. M., 2017, preprint, ([arXiv:1703.04542](https://arxiv.org/abs/1703.04542))
- Ross A. J., Brunner R. J., 2009, *MNRAS*, **399**, 878
- Rykoff E. S., et al., 2014, *ApJ*, **785**, 104
- Saito S., et al., 2016, *MNRAS*, **460**, 1457
- Scoccimarro R., Sheth R. K., Hui L., Jain B., 2001, *ApJ*, **546**, 20
- Seljak U., 2000, *MNRAS*, **318**, 203
- Sheth R. K., 2005, *MNRAS*, **364**, 796
- Sheth R. K., Tormen G., 1999, *MNRAS*, **308**, 119
- Sheth R. K., Tormen G., 2002, *MNRAS*, **329**, 61
- Sheth R. K., Tormen G., 2004, *MNRAS*, **350**, 1385
- Sheth R. K., Connolly A. J., Skibba R., 2005, *ArXiv Astrophysics e-prints*,
- Shi J., Wang H., Mo H. J., 2015, *ApJ*, **807**, 37
- Sin L. P. T., Lilly S. J., Henriques B. M. B., 2017, preprint, ([arXiv:1702.08460](https://arxiv.org/abs/1702.08460))
- Skibba R. A., Sheth R. K., 2009, *MNRAS*, **392**, 1080
- Skibba R., Sheth R. K., Connolly A. J., Scranton R., 2006, *MNRAS*, **369**, 68
- Skibba R. A., et al., 2012, *MNRAS*, **423**, 1485
- Skibba R. A., Sheth R. K., Croton D. J., Muldrew S. I., Abbas U., Pearce F. R., Shattow G. M., 2013, *MNRAS*, **429**, 458
- Smith A., Cole S., Baugh C., Zheng Z., Angulo R., Norberg P., Zehavi I., 2017, preprint, ([arXiv:1701.06581](https://arxiv.org/abs/1701.06581))
- Stark D. V., et al., 2016, preprint, ([arXiv:1610.06932](https://arxiv.org/abs/1610.06932))
- Takada M., et al., 2014, *PASJ*, **66**, R1
- Taylor E. N., et al., 2015, *MNRAS*, **446**, 2144
- Teklu A. F., Remus R.-S., Dolag K., Beck A. M., Burkert A., Schmidt A. S., Schulze F., Steinborn L. K., 2015, *ApJ*, **812**, 29
- Tinker J., Wetzel A., Conroy C., 2011, preprint, ([arXiv:1107.5046](https://arxiv.org/abs/1107.5046))
- Tinker J. L., Hahn C., Mao Y.-Y., Wetzel A. R., Conroy C., 2017, preprint, ([arXiv:1702.01121](https://arxiv.org/abs/1702.01121))
- Vakili M., Hahn C. H., 2016, preprint, ([arXiv:1610.01991](https://arxiv.org/abs/1610.01991))
- Vogelsberger M., et al., 2014, *MNRAS*, **444**, 1518
- Wang W., White S. D. M., 2012, *MNRAS*, **424**, 2574

- Wang W., Sales L. V., Henriques B. M. B., White S. D. M., 2014, *MNRAS*, **442**, 1363
- Wang J., et al., 2015, *MNRAS*, **453**, 2399
- Wechsler R. H., Zentner A. R., Bullock J. S., Kravtsov A. V., Allgood B., 2006, *ApJ*, **652**, 71
- Weinmann S. M., van den Bosch F. C., Yang X., Mo H. J., 2006, *MNRAS*, **366**, 2
- Welker C., Devriendt J., Dubois Y., Pichon C., Peirani S., 2014, *MNRAS*, **445**, L46
- Wetzel A. R., Tinker J. L., Conroy C., van den Bosch F. C., 2013, *MNRAS*, **432**, 336
- Woo J., et al., 2013, *MNRAS*, **428**, 3306
- Woo J., Carollo C. M., Faber S. M., Dekel A., Tacchella S., 2017, *MNRAS*, **464**, 1077
- Wu P.-F., Zahid H. J., Hwang H. S., Geller M. J., 2017, preprint, ([arXiv:1702.03323](https://arxiv.org/abs/1702.03323))
- Xu H., Zheng Z., Guo H., Zhu J., Zehavi I., 2016, *MNRAS*, **460**, 3647
- Yang X., Mo H. J., van den Bosch F. C., 2003, *MNRAS*, **339**, 1057
- Yang X., Mo H. J., van den Bosch F. C., 2006, *ApJ*, **638**, L55
- Yang X., Mo H. J., van den Bosch F. C., Pasquali A., Li C., Barden M., 2007, *ApJ*, **671**, 153
- York D. G., et al., 2000, *AJ*, **120**, 1579
- Zentner A. R., Hearin A. P., van den Bosch F. C., 2014, *MNRAS*, **443**, 3044
- Zhang Y., Yang X., Faltenbacher A., Springel V., Lin W., Wang H., 2009, *ApJ*, **706**, 747
- Zhang Y., Dietrich J. P., McKay T. A., Sheldon E. S., Nguyen A. T. Q., 2013, *ApJ*, **773**, 115
- Zhang Y., Yang X., Wang H., Wang L., Luo W., Mo H. J., van den Bosch F. C., 2015, *ApJ*, **798**, 17
- Zheng Z., et al., 2005, *ApJ*, **633**, 791
- Zhu G., Zheng Z., Lin W. P., Jing Y. P., Kang X., Gao L., 2006, *ApJ*, **639**, L5
- Zinger E., Dekel A., Kravtsov A. V., Nagai D., 2016, preprint, ([arXiv:1610.02644](https://arxiv.org/abs/1610.02644))
- Zu Y., Mandelbaum R., 2015, *MNRAS*, **454**, 1161
- Zu Y., Mandelbaum R., 2016, *MNRAS*, **457**, 4360
- Zu Y., Zheng Z., Zhu G., Jing Y. P., 2008, *ApJ*, **686**, 41
- Zu Y., Mandelbaum R., Simet M., Rozo E., Rykoff E. S., 2016, preprint, ([arXiv:1611.00366](https://arxiv.org/abs/1611.00366))
- van den Bosch F. C., Abel T., Croft R. A. C., Hernquist L., White S. D. M., 2002, *ApJ*, **576**, 21
- van den Bosch F. C., et al., 2007, *MNRAS*, **376**, 841
- van den Bosch F. C., More S., Cacciato M., Mo H., Yang X., 2013, *MNRAS*, **430**, 725
- van den Bosch F. C., Jiang F., Campbell D., Behroozi P., 2016, *MNRAS*, **455**, 158

This paper has been typeset from a  $\text{T}_{\text{E}}\text{X}/\text{L}^{\text{A}}\text{T}_{\text{E}}\text{X}$  file prepared by the author.